# Potential effects of chemo-mechanical interaction with calcite bearing faults on modeled induced slip during $CO_2$ storage in sandstone aquifers

By

K.J.R. van der Looij

To obtain the degree of Master of Science

at Utrecht University

August 2022

Student number: 5857309

Project duration: January 17, 2022 – August 19, 2022

Thesis supervision:

| | | |
|---|---|---|
| 1st. | MSc. S. Osinga. | TNO |
| 2nd. | Dr. A.R. Niemeijer | Utrecht University |

# Abstract

$CO_2$ storage in aquifers has the potential of storage capacities of up to 1.5 Gt in the Netherlands. In geomechanical modelling of the risk of seismicity upon $CO_2$ injection in aquifers, currently the potential of chemical weakening of faults is often not taken in account. Laboratory experiments or observations form natural analogues of $CO_2$ injection however suggest that the dissolution of $CO_2$, which causes a lowering of the pH, can result in the dissolution of calcite which can cause weakening of fault strength or frictional strength. In this study, the effect on seismicity of chemically weakening static friction, dynamic friction, or cohesion of calcite or calcite bearing fault gouge in the presence of dissolved $CO_2$ is tested. To test these effects, three existing codes are coupled to simulate $CO_2$ flow, stress changes and corresponding fault rupture. Injection and flow through the sandstone reservoir is modelled using flow simulator TOUGH-ECO2M, from which the spatiotemporal relationships of temperature, pressure and $CO_2$ saturation are taken. Corresponding stress changes are calculated from poro-elastic and thermo-elastic equations using inhouse software SRIMA (Seal and Reservoir Integrity Mechanical Analysis). The stress changes are then projected on a fault surface with predefined roughness using BSQuakeSim (Block-Spring earthQuake catalogues Simulator), which is a rupture model for induced seismicity following stress changes. $CO_2$ concentration is coupled in several simulations to the value of either static friction, dynamic friction or cohesion following simple linear relations to individually test the influence of $CO_2$ on the rupture timing, magnitude and frequency. This study found that poro-elastic stress changes, thermos-elastic stress changes and chemical weakening from $CO_2$ saturation variation individually contribute to destabilisation of a fault following different spatio-temporal relations. Chemical weakening mainly lowers the required thermo-elastic stress change to reach criticality but can also act as the triggering mechanism. Pressure changes and $CO_2$- calcite interaction affect the fault stability over a longer spatial extent than temperature changes. In the current simulation setup, faults are largely chemically weakened prior to the arrival of a cold front at the fault surface. It is found that lowering the static friction leads to earlier rupture events, a higher total number of rupture events but not necessarily of higher moment magnitude. Lowering the static friction increases the stress drop and thus stress release upon rupture. Therefore, rupture events of higher moment magnitude are found. Chemically lowering cohesion values leads to earlier rupture events, and a larger area of the fault surface along which slip occurs. Localized weakening of parts of a fault surface could affect the stability of the whole fault. In should be noted that to visualise changes in seismicity, initial criticality was required, therefore some unfavourable assumptions were made regarding injection rate and injection temperature. Also, the reactivity of calcite with the dissolved $CO_2$ is most likely overestimated in this study. However, under certain site-specific reservoir and injection conditions, localized fault strength weakening following $CO_2$ injection can contribute to the triggering of rupture events and magnitude of events and should therefore be taken in account in future seismic risk assessments of CCS projects in aquifers.

# Table of Contents

# Introduction

Concentrations of $CO_2$ in the Earth's atmosphere have reached alarming heights during the last decades. In 2018, a record amount of 33.5 Gt $CO_2$ was emitted worldwide related to the global energy supply. After an emission decline of 5.8% in 2020 during the Covid-19 pandemic, current emission levels are almost back at the 2018/2019 pre-Covid-19 level again (IEA, 2021). The surface average for carbon dioxide concentration from measurements at the remote NOAA (National Oceanic and Atmospheric Administration) sampling location at Mauna Loa was calculated at 414.4 ppm in 2020 (NOAA, 2021). The concentration of $CO_2$ is becoming increasingly closer to 450 ppm which is generally seen as a threshold for a 50% chance that the global average temperature rise will exceed 2°C with respect to pre-industrial times, potentially triggering irreversible damage to the climate. A global effort is being made to lower emissions, and local policymakers are setting out pathways to emit less $CO_2$. In the Netherlands, capture, transport, and storage of carbon dioxide produced by industry is regarded by the sector and national government as a crucial method for achieving the 2030 climate targets in a cost-effective manner (National Climate Agreement, 2019). As no $CO_2$ storage projects are currently active in the Netherlands in 2022, quick action is required to meet these targets. Key concerns in $CO_2$ storage are whether CCS is safe using current knowledge and techniques and whether the stored $CO_2$ will remain in the subsurface for over 10.000 years, in other words, whether the storage integrity is maintained.

## On $CO_2$ storage

Carbon Capture and Storage (CCS) is the process of capturing carbon dioxide emissions and either temporarily or permanently storing them deep below the earth's surface. Broadly speaking, 3 ways of storing $CO_2$ in the subsurface exist: 1) storage in carbonate reservoirs. 2) storage in porous saline aquifers. 3) storage in depleted gas or oil reservoirs. $CO_2$ is injected into the reservoir either as liquid, gas, or in a supercritical state depending on the injection temperature and pressure.

Usually, when considering $CO_2$ storage in the Netherlands, the focus is on depleted gas reservoirs (DGR). In this study, the focus will be on deep saline aquifers (DSA). If $CO_2$ storage is desired to adopt a major role in $CO_2$ emissions reduction, all potential ways should be explored and tested for safety. Another reason to focus on deep saline aquifers is their huge storage potential in the Netherlands. Assessment of the Dutch deep saline formations combined with seismic data and knowledge from proximal gas and oil activities resulted in a list of low-risk potential storage locations with a theoretical capacity of up to 1.5 Gt $CO_2$ in saline aquifers (Neele et al., 2013), which covers almost 10 times the total $CO_2$ emissions of 153.3 Mt (excl. land usage) in the Netherlands in 2019 (RIVM, 2021). A third reason to gain interest in the development of deep aquifers is the constantly increasing storage security. In gas fields, structural trapping remains the main way of trapping $CO_2$, which causes the potential for leaking to persist for a long time. In contrast, storage in saline aquifers results in the long-term trapping of $CO_2$ as a solute in water or as a component in precipitated minerals (IPCC., 2005) as shown in figure 1.

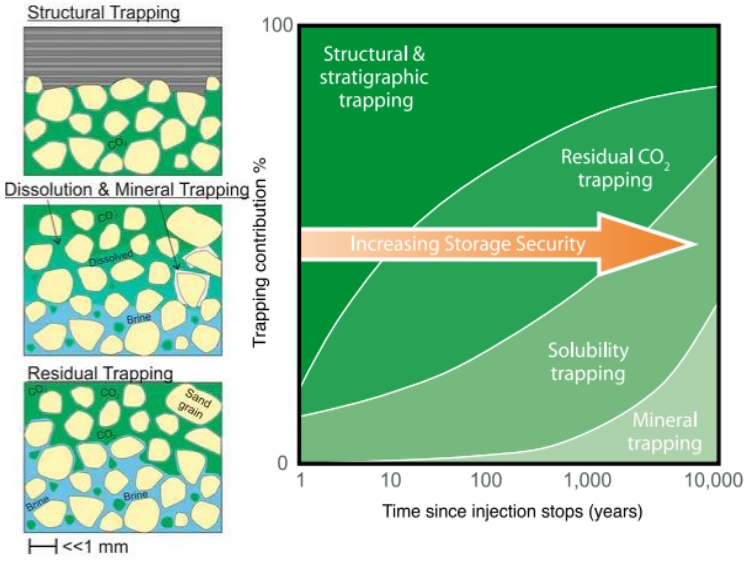


*Figure 1 Diagrammic illustration of the temporal contribution of different trapping mechanism to CO2 storage. This is a generalized idea and actual proportions will largely depend on site specific parameters as mineralogy and physical state of the reservoir. From IPCC. (2005)*

## Study objective

Observations from currently operational CCS sites indicate that induced seismicity is expected during injection operations, albeit to a limited extent in terms of seismic magnitude (e.g. Couëslan et al., 2014; Trupp et al., 2021; White & Foxall, 2016). Triggering of seismic events along pre-existing faults causing vibrations felt at the surface should be avoided. Also, activation of slip along faults that cross-cut seals poses a risk of $CO_2$ leakage. Risk assessment of $CO_2$ storage should consider hazards related to specific $CO_2$ injection and hazards concerned with any kind of fluid injection (White & Foxall, 2016). Fluid injection hazards could be the changing of pore pressure near/at fault zones, or perturbating far-field stresses leading to (a)seismic fault slip. In $CO_2$ storage, an additional hazard results from the fact that $CO_2$ is usually injected at different temperatures than the reservoir rock (e.g. Vilarrasa et al. (2019). Another hazard is the chemical influence of $CO_2$ on the pH, and mineralogy of the reservoir and pre-existing faults in the reservoir (Rohmer et al., 2016; Zhang et al., 2009).

The strength of pre-existing faults is determined by the effective normal stress on the fault, and static friction coefficient and the cohesion of the fault gouge, the wear product of the fault (van den Ende & Niemeijer, 2019). Upon rupture, cohesion is lost, and the friction coefficient switches towards dynamic friction. The step from static to dynamic friction is a complex, time-dependent step, and so-called rate and state parameters *(a-b)* determine whether unstable velocity weakening slip ($(a-b)<0$) or stable velocity strengthening slip ($(a-b)>0$) will occur upon slip (Dieterich, 1978, 1979; Ruina, 1983). To prevent introducing unconstrained complexities in the fault friction, an instantaneous slip weakening step between static and dynamic friction is assumed in this study.

The chemical influence of $CO_2$ on faults could include alteration of the fault gouge mineralogy or porosity. A decrease in static friction coefficient has been suggested to potentially result from the dissolution of the smallest grains within the fine-grained wear product of faults or particle roughness alteration in carbonate-rich rock (Rattez et al., 2021). Similarly, enhanced precipitation/ dissolution and alteration of porosity are suggested to influence the dynamic friction coefficient in carbonate rocks (Bakker et al., 2016; Bakker., 2017; Pluymakers et al., 2014; Rattez et al., 2021; Rohmer et al., 2016). Next to static or dynamic frictional strength, fault cohesion will be investigated. The cohesion of inactive fault gouge has been shown to increase during long periods of fault inactivity due to fluid-rock interactions (van den Ende & Niemeijer, 2019), yet cohesion could diminish significantly in the presence of $CO_2$ (Kim et al., 2018)

One way of predicting induced seismicity during or after $CO_2$ injection is by numerical modelling, which has been done in many different ways in the past (e.g. Rutqvist et al., 2014). In this study, models will be designed to simulate reservoir and fault behaviour considering suggested poro-thermo-chemo-mechanical effects during short- and long-term $CO_2$ storage. The focus will be more specific on the effect of an evolution of the fault friction and fault cohesion on the magnitude, frequency and timing of seismicity. The key questions are:

- What amount of frictional decrease, and/or cohesion loss can be expected as a result of reactions of calcite fault gouge with $CO_2$?
- Would the decrease in friction and/or cohesion be sufficient for fault reactivation in a generic scenario of $CO_2$ injection into a saline aquifer?
- Will induced seismic events be larger or smaller if fault strength is reduced by lowering friction versus removal of cohesion?
- What will be the main differences in effects of changing static friction, dynamic friction or cohesion on the seismicity?
- If only parts of the fault zone are affected by the $CO_2$ plume and pushed to fail, what would be the effect on the size of the induced events?

# Chemical background

## $CO_2$ reactivity

$CO_2$ is broadly injected in a few different host rocks and settings, these including fractured carbonate rocks or porous sandstone reservoirs. This study will only discuss the chemical influence of $CO_2$ on sandstone reservoirs. Injection in sandstone reservoirs is usually either done in depleted gas/oil fields or (saline) aquifers. Both require an initial stratigraphic or structural trap to contain the injected $CO_2$. In aquifers, the $CO_2$ will be distributed and over time become trapped within the rock formation as shown in figure 2. Chemical reactions play a huge role in the mineralogical and solubility trapping of $CO_2$.

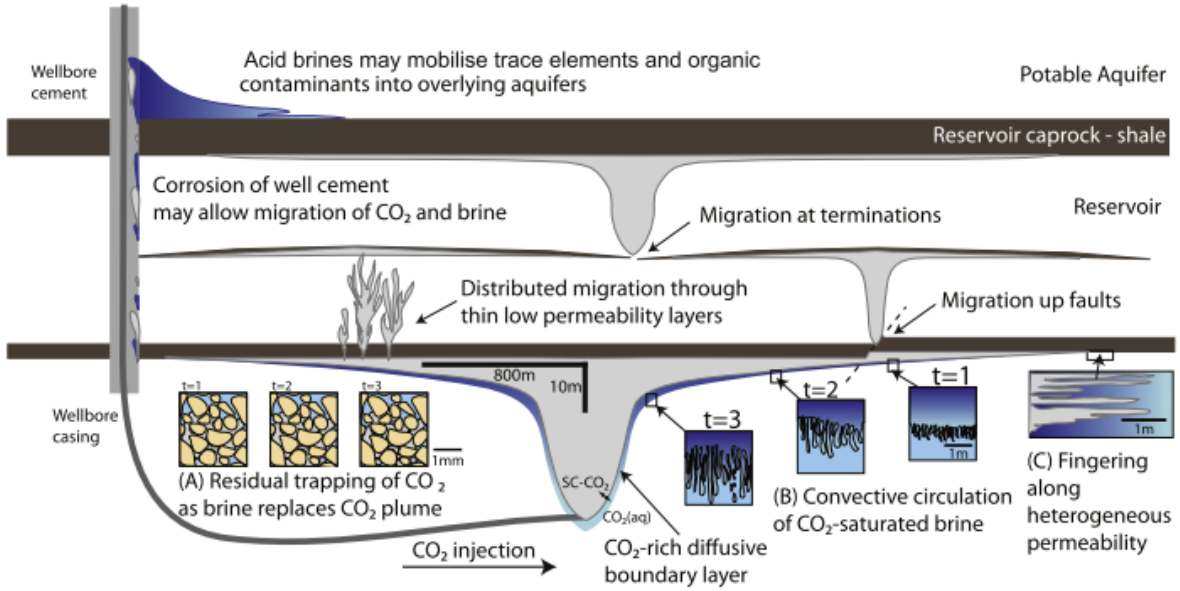


*Figure 2: Complete overview of trapping mechanisms and transport ways of $CO_2$ in reservoirs. Figure from Kampman et al. (2014)*

During injection of $CO_2$, we can subdivide the injection well and surrounding reservoir into 4 zones:

1. The volume near the wellbore is expected to be fully saturated with supercritical or liquid $CO_2$.
2. A transition zone with the presence of a 2-phase mixture of supercritical or liquid $CO_2$ and brine,
3. A zone that is initially fully saturated with acidified aqueous $CO_2$ solution, and $CO_2$ saturation diminishes with growing distance from the $CO_2$ plume.
4. Unaffected zone.

Most chemical reactions are found to take place in zones 2 or 3 (Rohmer et al., 2016) where $CO_2$ saturation in the brine leads to lowered pH as described below, which strengthens the idea that little geochemical effects are expected upon injection into the remaining gas of a gas field.

Geochemical studies have identified the key chemical processes occurring during $CO_2$ storage in sandstone reservoirs either by observing natural analogues (e.g. Bakker et al., 2016; Bickle et al., 2013; Hangx et al., 2015; Kampman et al., 2014) or experimental work (e.g. Bakker et al., 2016; Gaus, 2010; Hangx et al., 2013, 2009; Hangx & Spiers, 2009; Kampman et al., 2014; Marbler et al., 2013; Rattez et al., 2021). Several potentially significant chemical processes were identified influencing the host reservoir rock or fault gouge in remnant faults or fractures (Kampman et al., 2014): 1) Dissolution of $CO_2$ into the present water phase in the reservoir and a corresponding pH drop. 2) Mineral dissolution, buffering the pH, increasing porosity, and changing permeability. 3) Precipitation of several mineral types from solution as a result of the buffered pH, again influencing porosity and permeability. All chemical processes below are expected during injection in (saline) aquifers. The main trigger of

geochemical reactions during $CO_2$ sequestration is the formation of the acid $H_2CO_3$ upon dissolving in the brine (Gaus, 2010) as shown in equation 1:

$$CO_2 + H_2O \leftrightarrow H_2CO_3 \leftrightarrow H^+ + HCO_3 \quad (1)$$

which will cause a direct drop in the pH of the reservoir fluid, triggering an acid attack on surrounding minerals. Generally, the minerals that are directly affected by this acid attack are carbonate and Fe-Oxyhydroxide minerals (Kampman et al., 2014). Carbonate dissolution occurs through equation 2:

$$CaCO_3 + H^+ \leftrightarrow Ca^{2+} + HCO_3 \quad (2)$$

which will buffer the acid attack. The impact of these reactions (1 and 2) is determined by site-specific conditions: The pressure, temperature, mineralogy, grain size, spatial distribution of minerals, composition of the brine, water saturation and starting porosity and permeability (Gaus, 2010). As the combination of these factors is dependent on many variables, no general set of rules exists to date that applies to a wide range of basins, and site-specific geochemical modeling is required.

In carbonate cemented rocks, the dissolution of Carbonate and Fe-Oxyhydroxide minerals are followed by more sluggish reactions with silicates and phyllosilicates (Hangx & Spiers, 2009; Kampman et al., 2014). Again, these reactions will buffer the acid attack and increase the pH. These reactions take place over a timespan of days to weeks and lead to increased concentrations of anions/cations in solution (L. Zhang et al., 2019).

The buffered pH will result in a changed chemical equilibrium (assuming no influx of new acidity), which in turn promotes carbonate precipitation over a timescale of weeks to months. Fe-Mg-Ca carbonate mineral precipitation will occur, for which the dissolution of silicate minerals and transport of $CO_2$-charged brines are the rate-limiting step. In other words, either the supply of acidity in close to chemical equilibrium situations is rate-limiting, or silicate-mineral reactions are rate-limiting by the surface reaction with brines far from equilibrium and not limited by the supply of acidity (Kampman et al., 2014). Whether an open system is expected with relatively fast $CO_2$ flow or a closed system close to chemical equilibrium depends on the in-situ conditions.

Combinations of dissolution of minerals near the injection point and precipitation at a more distal point can potentially result in spatial permeability and porosity changes. Numerical simulations showed that the extent of reactions correlated to $CO_2$ storage is highly dependent on the initial rock type and mineralogy (e.g. Xu et al., 2004). Another factor that determines the way calcite behaves in reactions (dissolving or precipitating) is the pH of the fluid (Lagneau et al., 2005) as the solubility of calcite is a lot higher at low values for pH. Finally, the temperature and pressure conditions at which the injection occurs determine the amount of soluble $CO_2$, reaction rate, and thus the extent of the chemical reactions (e.g. Duan & Sun, 2003).

Changes in porosity and permeability were mentioned both in sandstones with carbonate cement (e.g. Hangx et al., 2013; Marbler et al., 2013) as a result of carbonate mineral dissolution or, to a lesser extent in sandstones with silicate cement (Lamy-Chappuis et al., 2013; Nover et al., 2013; Rimmelé et al., 2010) resultant from clay mineral dissolution. The change in porosity is a combination of dissolution (increase), particle removal (increase), precipitation (decrease), or mechanical compaction (decrease) (Rohmer et al., 2016). General empirical equations describe how a change in porosity is usually linked to a change in unconfined compressive rock strength (Chang et al., 2006). Permeability of the rocks is noted to change as a result of a complex interplay between mineral dissolution/precipitation and pore clogging by fine particles. An increase in permeability can be found beneficial as larger permeability leads to lower pore pressure changes with injection. Again, the extent of the porosity and permeability changes is highly dependent on pH and thus whether an open or closed system is observed.

# Fault strength background

## Friction and cohesion

Usually, the first locations within rocks that are expected to fail, and thus lead to any seismicity are pre-existing faults. Whether fault reactivation occurs can be determined using the Mohr-coulomb failure criterion:

$$\tau = S_0 + \mu\sigma_n^{eff} \qquad (3)$$

in which τ represents the shear strength, $S_0$ represents cohesion, $\sigma_n^{eff}$ represents effective normal stress and $\mu$ represents the fault friction coefficient. Influencing any of the parameters of equation (3) will affect fault stability, as shown in figure 3.

The effect of $CO_2$ on frictional strength and properties of faults zones and gouge has been evaluated in both laboratory experiments (short timescale) as well as in natural analogues (long timescales). Experimental work on long-term effects is limited (e.g. Hangx et al. (2015)), mainly because of the slow, time-consuming reactions.

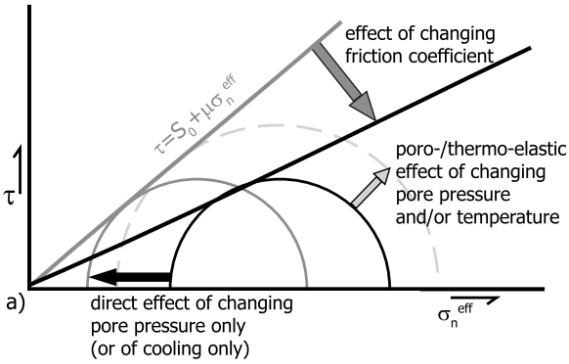


*Figure 3: the Mohr-Coulomb type failure criteria and the possible effects of CO2 injection on this criterion. Figure taken from Pluymakers et al. (2014).*

Calcite gouges, are expected to be influenced by the presence of $CO_2$, following the reactions in equations 1 and 2. Much of the experimental work is focused on the velocity dependence of friction of fault gouge, i.e. the frictional stability which is thought to control whether seismic or aseismic slip occurs (e.g. Pluymakers et al. (2014); Samuelson & Spiers, (2012)). It is beyond the scope of this study to consider the velocity dependence. This study focuses on whether faults will be reactivated at all considering changes in stress and fault strength.

The strength of an inactive fault is determined by the restored friction coefficient and the restored cohesion resulting from fault healing during periods of inactivity (Hunfeld et al., 2020; Tenthorey & Cox, 2006; van den Ende & Niemeijer, 2019). Cohesion is found to restore largely through cementation and overgrowths, whereas static friction coefficient largely increases through an increase in contact area. Such contact area can be increased due to asperity growth or compaction (Chen et al., 2015). Whether time-dependent healing of cohesion or static friction contributes most to fault stability depends on the effective normal stress (van den Ende & Niemeijer, 2019).

## Chemical effects on friction

Experimental work on the long-term effects of calcite dissolution within a clay-calcite mixed fault gouge showed that gouges leached of any calcite due to dissolution showed a decrease of ~10-15% in dynamic friction ($\mu_d$) value with respect to their non-leached counterparts (Bakker and Spiers, 2013). These authors, however, also found that reprecipitation of other minerals like kaolinite could lead to an increase in $\mu_d$ values, depending on the initial clay-calcite ratios.

Rattez et al. (2021) found that for the long-term effects of $CO_2$, carbonate gouge is also affected. Again, in the worst-case scenario, if an unlimited supply of flowing $CO_2$-saturated water is available, they reported that up to 25% of the gouge material can dissolve. Mainly the smaller particles would be dissolved, influencing the particle size distribution, porosity, and permeability. These authors also found that the peak frictional strength (static friction $\mu_s$) and the residual frictional strength (dynamic friction $\mu_d$) decreased at higher levels of degradation and dissolved calcite gouge.

Fracture surface roughness has also been found to decrease by chemical alteration as the result of an acidic fluid flowing through a fracture (Nouailletas et al., 2013). The chemical attack would lead to material removal, the disappearance of asperities, and a lowered peak shear strength. The degraded samples showed the behavior of a smooth joint rather than a rough fracture.

Pluymakers et al. (2014) found through direct shear experiments that for anhydrite gouge, the dynamic friction coefficient of the gouge can be reduced by 4-15% in the presence of water and $CO_2$. A requirement for such reduction is a scenario where unlimited supply of $CO_2$ can flow freely through the gouge material (open system). Their study suggested that this reduction is due the microscale dissolution of asperities in anhydrite grain contacts or shear bands and accompanying precipitation of calcite, which also has the potential to reduce the dynamic friction coefficient (Pluymakers et al., 2014). Similar processes could apply to calcite as well.

(Pluymakers et al., 2014) also suggested that enhanced precipitation of calcite associated with anhydrite dissolution could decrease the fault porosity as the molar volume of calcite exceeds that of anhydrite. Bakker et al. (2016), however, stated that significant changes in frictional strength of faults in a $CO_2$ storage system resulting from such precipitation are only expected when there is major carbonate precipitation in the fault damage zone due to rapid $CO_2$ leakage and degassing.

### Chemical effects on cohesion.

Next to friction coefficient change, a decrease in cohesion is a potential consequence of $CO_2$ storage. Experimental rock strength and direct shear experiments on natural analogues of long term $CO_2$ alteration (Hangx et al., 2015) showed that for specific zones within the altered rock, certain zones showed a strength up to 1/3 lower than less altered parts of the reservoir. Enhanced anhydrite dissolution from these mm-sized zones led to higher porosity and lower rock strength. The anhydrite cement would be present as randomly distributed nodules filling pores and contributing to the rock framework strength but to a spatially very limited extent. These high porous zones also showed a cohesion value lower than the unaffected reservoir sandstones (16.8 MPa versus 22.7 MPa). Although in the study of (Hangx et al., 2015) focused on anhydrite dissolution, similar processes and weakening of the rock can apply for calcite dissolution.

Experimental work by Marbler et al. (2013) and Erickson et al. (2015) showed similar results. They performed triaxial tests on sandstone rocks that had been artificially altered by being exposed to supercritical $CO_2$ + brine for up to 1 month. These authors showed that the exposure of either pure supercritical $CO_2$ or supercritical $CO_2$ mixed with impurities ($SO_x$, $NO_x$, and $O_2$) in such altered rocks can lead to mean lowered elastic constants of 10-40% both for siliceous cemented sandstones as for carbonate cemented sandstones. In carbonate cemented sandstones a decrease in uniaxial compressive strength (34.1 to 11.1 MPa) and cohesion (7.5 to 1.9 MPa) was found. Both the decrease in elastic properties as well as the decrease in strength are attributed to the progressive alteration of carbonate minerals within the matrix of the carbonate sandstones.

Within calcite cemented sandstones, the study by (Lamy-Chappuis et al., 2016) found that both the yield stress and the peak stress diminishes as more calcite dissolves. Their experimental setup is hard to compare to other studies, as multiple failure tests were conducted on a single sample, resulting in an overall lower value of strength. Their study, however, did not experience any problems related to sample heterogeneity and clearly showed that dissolution of 4.5 mass% calcite affected the peak strength by lowering the cohesion from 14.5 to 10.5 MPa and internal angle of friction from 16.0 to 8.3°, thus lowering the shear strength.

Experimental work by Zhang et al. (2020) found that the addition of supercritical $CO_2$ to initial brine saturated sandstone affected the micromechanical properties of sandstone quite substantially. The authors reported on Illite dissolution and kaolinite precipitation from microstructural analysis. They proposed a microphysical model for crack initiation induced by $scCO_2$ – water- rock interaction that

takes in account cohesion, friction and tensile fracture toughness. Using their model, they reported on a compressive strength reduction of 7.1% and 13.0% for 15 days and 30 days saturation periods respectively. Compared to initially water saturated samples, the $scCO_2$-water saturated samples show a reduction of 15% and 37.3 % for 15 days and 30 days saturation respectively.

However, other experiments showed no notable change in experimental strength after $CO_2$ alteration (e.g. Canal et al., 2014; Hangx et al., 2013). Yet this could be the result of carbonate not being part of the load-bearing framework of the rock. The amount of change in mechanical strength of a rock depends on the sedimentation and diagenesis of the rock. If the dissolving minerals are part of the load-supporting framework, the $CO_2$ injection will lead to a lowered rock strength (Hangx et al., 2015).

# Methods and workflow

To enhance potential future application of this study, and to increase credibility, the properties of an existing aquifer that is a potential target for $CO_2$ storage in the Dutch subsurface are mimicked: the lower Cretaceous "IJsselmonde sandstone reservoir" in the P18 block. An earlier initial feasibility study was conducted on the Lower Cretaceous sandstone reservoirs above the P-18 gas field (Geel et al., 2021). Properties from their feasibility study and other studies concerning the Jurassic sandstone under burden, IJsselmonde sandstone reservoir and Vlieland Shale caprock have been used as input for the research codes used in the workflow. An overview of these properties, their values and data source are provided in table 1. The IJsselmonde sandstone member is a shallow-marine sandstone, which contains intercalated claystones, considered to be back barrier lagoonal deposits. The porous sandstone is calcareous cemented and locally contains shells and shell fragments (TNO-GDN (2022)). No clear mineralogy was found in literature so a similar calcite mass-percentage of 25% as the opalinus claystone (OPA) used in the study of Bakker (2017) is assumed in this study. As reactive modelling is not part of the workflow, it is assumed that the rest of the rock mass (75 mass%) does not react. The mineralogy of the fault gouge modelled is either assumed to be similar to the OPA rock or assumed to be pure (i.e., 100%) calcite (further specified below).

This study is divided into three parts contributing to the overall workflow. The modelling will involve three components: (i) flow, (ii) induced stress, (iii) induced seismicity. A combination of analytical and semi-analytical pre-existing approaches is used to model these 3 components. Each part of the workflow is performed through the utilization of different software packages and the workflow spans both Fortran as well as MATLAB based programs and scripts. Combined, the programs form a workflow for answering the key questions in this study.

## THOUGH2-ECO2N Module, flow simulation

Initially a clear image needs to be provided on spatial evolution of the liquid and aqueous $CO_2$ phase once injected in a porous aquifer with known properties. THOUGH2-ECO2M is a module of the flow simulator TOUGH2, specifically designed for applications of $CO_2$ storage in saline aquifers. THOUGH2 is a Fortran based numerical simulator for the calculation of flow of multiphase and multicomponent fluids in porous and fractured media (Pruess et al., 1999). The ECO2M module is an addition to the simulator containing the thermodynamic and thermophysical properties of H2O – NaCl – $CO_2$ mixtures within saline aquifer conditions (Pruess, 2011).

The simulator requires the input of a 2D mesh and assumes radial symmetry. It is specified what coordinate points lie within the caprock, reservoir rock and under burden in the mesh. Also, it is defined in which of the coordinate points supercritical $CO_2$ is injected in the mesh. In this study, the reservoir is defined by 23 points in the Z-direction (depth) and 47 points in the R direction (radius), creating a grid of 1081 points (see fig 5). These points are also the points at which data values (Pressure, Temperature, Saturation) are calculated during the simulation and at which those will be exported. Any values required in between these points are later interpolated using the standard MATLAB 'spline' interpolation, which is based on finding a mathematical function describing a smooth curve passing

exactly through the input point values. A reservoir mesh is created using a MATLAB script which exists of broadly 3 layers: under burden, reservoir and cap rock with relative thicknesses of 65, 100 and 65 m. Mesh points are selected such that near the borders of the reservoir, the point density is higher, thus increasing data resolution around the reservoir borders.

Second, the simulator requires an input text file containing the rock properties, injection fluid properties, and data on pressure and temperature in a predefined format. It must be specified where initially water, $CO_2$ or a mixture is found and in what phases these are initially present. The text file containing all start variables for the TOUGH2 simulation can be found in appendix 1. Further information about the data structure of TOUGH2 can be found in the manual of TOUGH2 (Pruess et al., (2012)) and the manual of the ECO2M module (Pruess, 2011). Relevant parameters are shown in Table 1.

| | **Density[a] (kg/m3)** | **Porosity [c] (%)** | **Permeability horizontal ($m^2$)** | **Permeability vertical ($m^2$)** | **Avg Pressure [f] (Pa)** | **Avg Temperature[g] (°C)** |
|---|---|---|---|---|---|---|
| **Caprock Vlieland Shale** | 2650 | 0.5 | 9.90E-19 | 9.90E-24 | 2.360E+07 | 77.0 |
| **Reservoir rock IJsselmonde Sandstone** | 2500 | 25.0 | 9.87E-13[d] | 9.87E-13[e] | 2.361E+07 | 78.8 |
| **Under burden Upper Jurassic Sands** | 2100 | 0.5 | 9.90E-19 | 9.90E-24 | 2.459E+07 | 80.8 |
| **Injection rock IJsselmonde sandstone** | 100000[b] | 25.0 | 9.87E-13 | 9.87E-13 | 2.361E+07 | 20.0 |

*Table 1: table containing input variables for TOUGH flow simulations. [a] Densities taken from Geel et al., 2021. [b] Extremely large value taken to keep the rocks at the injection well at constant T = 20°C. [c] Porosities taken from Geel et al., 2021 . [d]Permeability taken from* Geel et al., 2021 *. [f] Pore pressures calculated using average density of water * depth * gravitational constant. [g] Temperature calculated using average temperature gradient at the well's location, taken from (Harper, 1971)*

An injection temperature of 20° C is adapted, which is similar to the injection temperature used in the study of Vilarrasa et al. (2019). A combination of aqueous and liquid or supercritical $CO_2$ is expected in the water- $CO_2$ system, which means that no gaseous $CO_2$ phase is expected in the reservoir as a result of the high pore fluid pressure keeping the injected $CO_2$ in a liquid or supercritical state (see figure 4). In TOUGH, for supercritical temperatures ($T > T_{crit} = 31.4°C$), $CO_2$ is arbitrarily assigned the single $CO_2$-rich "liquid" phase when $P > -P_{crit} = 7.38$ MPa and "gas" when $P < P_{crit}$. As of choice of the injection temperature, no gaseous nor solid $CO_2$ phase is expected during simulation. The choice of injection temperature determines the temperature changes and thus largely affects the thermo-elastic stress changes in the reservoir. Therefore, injection temperature is kept constant through all simulations, as determining the thermos-elastic stresses is not the main goal of this study. Any liquid water is ascribed as the aqueous phase in the model. The actual amount of $CO_2$ present in the water can be found by multiplying the fraction of aqueous water with the mass fraction $CO_2$ in the aqueous phase times the density of the pore fluid (all output variables from TOUGH). The simulator does not consider further reactions between $CO_2$ and the rock minerals.

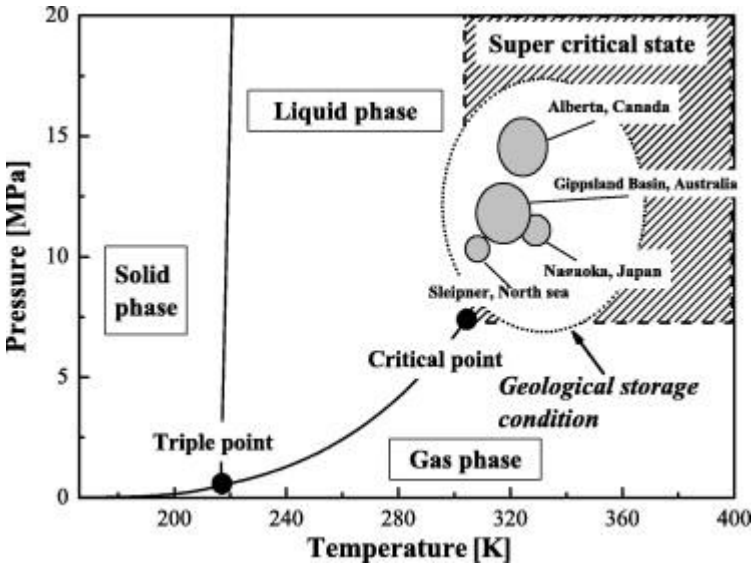


*Figure 4: PT diagram of the state of CO2 at varying Pressures and Temperatures. Plotted in the graph are some locations around the word in which CO2 injection in a supercritical state is performed (from Sasaki et al. (2008))*

An injection rate of 4 Mt/year is chosen as it leads to seismicity using the workflow and assumptions in this study. Initial criticality is a requirement in order to test the effects of varying different parameters in BSQuakeSim, the software used to model rupture (further explained below). Initial test runs at an injection rate of 1 Mt/year or 2 Mt/year did not lead to any rupture events when testing the workflow without any $CO_2$ influence. Normally, an average injection rate of 1 Mt/year would be a more general accepted minimum injection rate that a $CO_2$ injection well should be capable of to be economically valuable (Van der Meer & Yavuz, 2009). The choice to use an injection rate of 4Mt/y is thus expected to have a large influence on the absolute values of pressure increase, and spatial extent of the $CO_2$ plume and temperature front. However, as the injection rate is kept similar through all simulations, relative chemical effects can still be tested. The injection rate is divided over the length of the injecting column of 100 m.

Initially, the reservoir is generated, and a simulation is run for 50 years without injection to minimalize any steps in pressure or temperature resulting from the uniform temperature and pressure that are initially assigned to the base/cap rock and reservoir. The output from the initial simulation is used as input for the injection run. The injection run spans a duration of 50 years of injecting 4Mt/year. In total 200 Mt $CO_2$ is injected, which is in the order of > 4 times the estimated storage capacity of individual compartments of the aquifer in the P-block (Neele et al., 2012), but in the same order magnitude as the Q-block aquifer connecting several oil fields with a total estimated storage potential of 135-235 Mt (Neele et al., 2013). Data is exported on all timesteps provided in the input file and on timesteps that are relevant timestep according to the TOUGH program. Over 140 timesteps are exported among which an exported timestep at exactly each full year after the start of injection. The output of interest for this study is the spatial distribution of the temperature front, pressure increase and $CO_2$ saturation

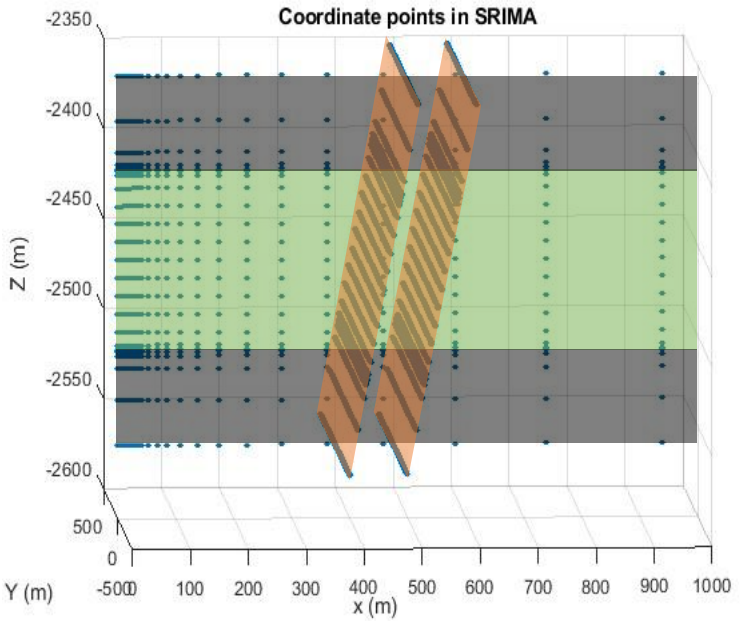


*Figure 5: Coordinate points on which at every timestep P, T conditions and $CO_2$ saturation is provided by TOUGH. Points on the Y=0 represent output from TOUGH. The grey area represents under burden/cap rock, the yellow area represents reservoir rock. Points perpendicular to the X-Z plane represent fault coordinates at which data is interpolated prior to SRIMA's stress calculation. The red area represents the faults. Injection is done at Y=0, X = 0 within the depth limits of the reservoir.*

resulting from injection. After 50 years of injection, the run is manually restarted for another 50 years but without injection. During these 50 years, the $CO_2$ present in the aquifer will continue to move solely as result of convective circulation and dissolution.

A MATLAB script is constructed to read the TOUGH output file into MATLAB variables. The output of TOUGH is provided as 2D results representing a radial symmetric reservoir and coordinates are provided in radius (r) and depth (Z). As this study is focused on the potential reactivation of pre-existing faults, a second script adds coordinate points describing a fault in the reservoir with desired depth (spanning the whole TOUGH simulation), width (1000 m) and a dipping angle of 60°. The P, T, and $CO_2$ saturation-values are interpolated horizontally from the TOUGH output using spline interpolation and exported on cartesian (X, Y, Z – coordinates). Initial test runs indicated that the cold front is expected to gradually end around 500 m distance from the injection well. Therefore a fault is created for which the top part is at 500 m distance from the injection well and a second simulation is created with the fault at 600 m from the injection well, just outside of the cold front. Initial tests showed that a fault of which the top part is located at 650 m would not lead to initial criticality in BSQuakeSim. Figure 5 shows the location of both the proximal TOUGH output coordinates and the fault coordinates. The P, T-values, timesteps, and coordinate points are stored in a standard MATLAB file format which can be read by SRIMA (a tool used next in the workflow, as further explained below). Saturation values on the fault plane are exported to 101 timesteps with $\Delta t = 1$ year (timestep 1 is at t=0). The saturation values are exported to a separate file that can be loaded in Block-Spring, which is the software that is used later in the workflow to model rupture resulting from stress changes.

## SRIMA, stress changes calculation

SRIMA (Seal and Reservoir Integrity Mechanical Analysis) is a semi analytical tool used for calculating the stresses on faults and within a reservoir resulting from injection (Buijze et al., 2021). The program is based on a simple geometry with radial symmetric injection fronts, temperature and pressure field. The tool requires an initial state of stress (not radially symmetric) and data files containing the pressure and temperature at each timestep and at each coordinate point

The initial state of stress is calculated from an initial horizontal and vertical stress at the top of the under burden, reservoir and cap rock and a constant stress gradient, $d\sigma/dz$. These values, other relevant parameters and sources are shown in table 2. To simplify the stress calculations, in the initial state $dP/dz$ is taken as 0, and pore pressure values are assigned to the under burden, reservoir rock and cap rock similar to those shown in table 1 above. Permeability and porosity values are taken to be the same as the TOUGH simulation values. Other required input variables are calculated where possible or taken as standards values when no data could be found (table 2)

Next, the output coordinate points from TOUGH and their respective values for pressure and temperature for each timestep are required. These are provided in a standard format containing arrays for pressure (‘P’), temperature (‘T’), coordinate points (‘noder’ and ‘nodez’ for horizontal and vertical position) and times in days (‘alltimed’). The program will calculate up to 10 concentric circles describing the radial $\Delta T$ and $\Delta P$. Elevated pressures alter the total stresses through poro-elastic effects, and the effective stresses through the pressure change itself. Meanwhile, temperature changes also induce a change of the total stress. A stress field and change in stress field is calculated at every timestep using poro-elastic and thermo-elastic equations. The program next calculates effective stress changes and recalculates the stresses and stress components from radial coordinates to cartesian coordinates using standard matrix transformations. Export of data is possible from the SRIMA GUI, which contains all values of P, T, effective stresses, stress changes and the full stress tensor. These stress values are a required input for BSQuakeSim, which is used to simulate the slip that might result from the stress changes upon injecting $CO_2$.

| Variable | Value | Unit | Data source |
|---|---|---|---|
| **Vertical stress gradient $d\sigma_v/dz$** | 32.42 | MPa/km | Calculated from total weight of overburden |
| **Stress ratio $\sigma_h/\sigma_v$** | 0.67 | | $d\sigma_v/dz$ calculated, $d\sigma_h/dz$ from (Bakx, 2022) |
| **$d\sigma_h/dz$ caprock** | 21.72 | MPa/km | calculated from stress ratio and vertical stress gradient |
| **Stress ratio $\sigma_h1/\sigma_h2$** | 1 | | No horizontal stress anisotropy assumed |
| **$\sigma_v$ top Seal** | 75.71 | MPa | Calculated from Geel et al. 2019 |
| **$\sigma_v$ top Reservoir** | 77.80 | MPa | Calculated from Geel et al. 2019 |
| **$\sigma_v$ top Base** | 81.04 | MPa | Calculated from Geel et al. 2019 |
| **$\sigma_h$ top caprock** | 50.72 | MPa | calculated from stress ratio and vertical stress |
| **$\sigma_h$ top Reservoir** | 52.13 | MPa | calculated from stress ratio and vertical stress |
| **$\sigma_h$ top Base** | 54.30 | MPa | calculated from stress ratio and vertical stress |
| **Young's modulus (reservoir)** | 2.30E+4 | MPa | Calculated using formulas from Muntendam Bos (2008) |
| **Young's modulus (caprock)** | 1.34E+4 | MPa | Calculated using formulas from Muntendam Bos (2008) |
| **Young's modulus (under burden)** | 2.30E+4 | MPa | Calculated using formulas from Muntendam Bos (2008) |
| **Poissons ratio (reservoir)** | 0.17 | (-) | SodM, (2018) |
| **Poissons ratio (caprock)** | 0.20 | (-) | SodM, (2018) |
| **Poissons ratio (under burden)** | 0.17 | (-) | Assumed equal to reservoir |
| **Biot coefficient** | 0.81 | | SodM, (2018) |
| **Mohr-coulomb cohesion** | 5.90 | MPa | Calculated using data from SodM, (2018) |

*Table 2: Input variables required for SRIMA and their data source*

## BSQuakeSim, rupture simulation

Ultimately, the focus of this study is on the question whether the chemical effects resulting from $CO_2$ injection will affect the reactivation of faults. BSQuakeSim (Block-Spring earthquake catalogs Simulator) is a rupture model for induced seismicity in the context of stress changes resultant from geothermal systems (Candela et al., 2019). Stress changes are largely similar for geothermal injection or $CO_2$ injection. Therefore, BSQuakeSim can be used as a base for this study with some adaptions: the spatial $CO_2$ (aq) concentration is linked to the spatial dissolution of calcite, and the fraction of dissolved calcite is on its turn linked to the value $\mu_s$, $\mu_d$, or cohesion as shown below.

The export from SRIMA is slightly adapted such that the coordinates from the TOUGH output (located on the X-Z plane in figure 5) are removed and only the stress tensors, pressure and temperature at the fault coordinates are imported in the model. Next, $CO_2$ saturation values on the fault plane are imported. Initially, the stress values on the fault surface coordinates are interpolated to obtain triangular shaped patches. These patches follow the initial surface, but the triangular geometry allows for a 3-D roughness to be added to the fault surface to mimic faults more realistically. Parameters describing the roughness are kept similar in all simulation as roughness is not the key tested parameter in this study.

The stress values on the triangular patches are combined with an "instantaneous" slip-weakening model with initially spatial homogenous static ($\mu_s$) and dynamic ($\mu_d$) friction coefficient. In this study, a value of cohesion is added to the model. For each timestep (dt = 365.25/10 days), all triangular patches are checked for criticality following the coulomb failure criterion:

$\tau_s = \mu_s \sigma_n + S_0$ (4)

in which $\tau_s$ is the local effective shear stress, $\sigma_n$ is the local effective normal stress and $S_0$ is the local cohesion on the patch. When local shear stress reaches the failure criterion on a certain patch, a rupture is initiated, and the shear stress on that patch drops to:

$\tau_s = \mu_d \sigma_n$ (5)

Where the dynamic friction coefficient is adapted and cohesion is lost, i.e., is zero. The stress drop is visualized in figure 6. The stress drop equals the difference in shear stress between the static and dynamic system and is recalculated to a certain amount of slip along the patch. The slip distance along a patch correlated to a certain stress drop differs for each patch and is dependent on the orientation of the patch with respect to the main stresses. Slip along an initial patch releases a certain amount of long-range stress on the other parts of the fault surface. The long-range elastic stress interactions between the fault elements are accounted for via elastic Green's (or influence) functions for triangular dislocations (Nikkhoo and Walter, 2015). Again, for each patch the failure criterion is tested and all patches that are now prone to slip are added to the rupture event. The rupture cycle continues until all patches that satisfy the failure criterion are added to the single rupture event (Candela et al., 2019). Once all patches prone to rupture are added to the event, the moment magnitude (Mw) of the rupture event is determined from the shear modulus, total slipped area of the patches and the mean slip along a patch as such:

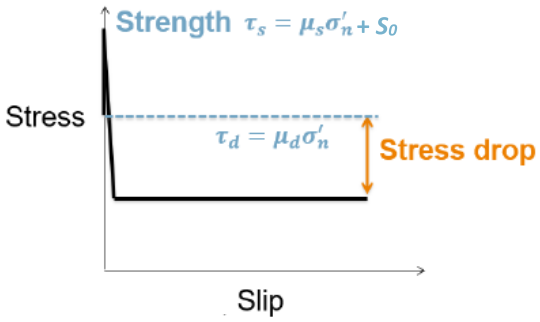


*Figure 6: "instantaneous" slip weakening model originally used in Block-spring. In this study cohesion is added to the strength prior to rupture. (Adapted from Candela, 2019)*

$$Mw = \frac{\log10(mean\ slip\ distance \times shear\ modulus \times rupture\ area)}{1.5} - 6.06 \qquad (6)$$

In which the shear modulus is taken as 3.3 x $10^4$ MPa and the correction factors from seismic moment ($M_0$) to moment magnitude (-6.06 and 1.5) are taken from Purcaru and Berckhemer (1978). The model then proceeds to the next timestep.

After rupture, instantaneous healing of the frictional strength is assumed. The cohesion that was added in this study is not restored after rupture and remains "zero" at a slipped patch for the rest of the simulation (i.e. no time dependent healing of cohesion as suggested by (van den Ende & Niemeijer, 2019)). Another adaption in this study is that static Friction ($\mu_s$), dynamic friction ($\mu_d$) and cohesion ($S_0$) are made non-uniform and time dependent. For every timestep, values of the 3 variables are recalculated and new values are brought in the criticality calculations. The 3 variables can be externally altered over time, as is desired to test the chemical effects of the local $CO_2$ concentration on $\mu_s$, $\mu_d$, and $S_0$. At any spatial location the aqueous $CO_2$ concentration and density are known, which are easily translated to a molar reaction ratio of $CO_2$:$CaCO_3$ equalling 1:1 as shown in the reactions below.

$CO_2 + H_2O \leftrightarrow H_2CO_3 \leftrightarrow H^+ + HCO_3$ (1)

$CaCO_3 + H^+ \leftrightarrow Ca^{2+} + HCO_3$ (2)

Which shows that for every mol of $CO_2$, a mol of calcite will dissolve. As accurate dissolution rates of $CO_2$ and reaction rates of calcite are highly site specific and thus unknown in this study (e.g. (Gaus, 2010; Kampman et al., 2014) assumptions have to be made. In this study it is assumed that the **total** removal of calcite at a certain location corresponds to the **maximum** concentration of $CO_2$ that has passed a certain spatial location. In other words: once $CO_2$ (aq) concentration is increased at a location at a certain timestep, the amount of calcite at that location is instantaneously lowered. However, when $CO_2$ concentration is lowered again at the same location, the amount of calcite at that location remains equal. This assumption certainly affects the absolute amount of calcite dissolution, but in a similar way

for all simulations. The percentage of dissolved calcite is on its turn linked to either $\mu_s$, $\mu_d$, or cohesion as described below.

## Simulations setup

Initially a base case scenario is run (simulation 1 in table 3), in which no $CO_2$ effect on any of the variables is tested. In the base case simulation, an initial criticality is required as accurate comparison of the amount and magnitude of rupture events is not possible if not all scenarios experience rupture events.

| Simulation | Effect on | $\mu_s$ max | $\mu_s$ min | $\mu$ drop | $\mu_d$ max | $\mu_d$ min | $S_0$ min (MPa) | $S_0$ max (MPa) | Data source for calcite versus fault strength relationship |
|---|---|---|---|---|---|---|---|---|---|
| **1** | **no** | 0.5 | 0.5 | 0.15 | 0.35 | 0.35 | 1 | 1 | Bakker (2017) |
| **2** | $\mu_s$ | **0.5** | **0.36** | 0.15-0.05 | 0.35 | 0.35 | 1 | 1 | Rattez et al., (2021) |
| **3** | $\mu_d$ | 0.5 | 0.5 | **0.15-0.35** | **0.35** | **0.15** | 1 | 1 | Rattez et al., (2021) |
| **4** | $\mu_d$ | 0.5 | 0.5 | **0.15-0.23** | **0.35** | **0.27** | 1 | 1 | Bakker., (2017) |
| **5** | $\mu_d$ | 0.5 | 0.5 | **0.15-0.10** | **0.35** | **0.4** | 1 | 1 | Bakker., (2017) |
| **6** | $S_0$ | 0.5 | 0.5 | 0.15 | 0.35 | 0.35 | **1** | **0** | Lamy-Chappuis et al., (2016) |
| **7** | $S_0$ | 0.5 | 0.5 | 0.15 | 0.35 | 0.35 | **10** | **0** | Lamy-Chappuis et al., (2016) |

*Table 3: Parameter setup for systematically testing the effect of $CO_2$ (aq) on $\mu_s$ = Static Friction, $\mu_d$ = dynamic friction, $\mu$ drop = $\mu_s - \mu_d$, and $S_0$ = Cohesion. The right column contains the study from which the respective data on percentile decrease of either $\mu s$, $\mu d$, or S0 upon dissolution of a certain amount of calcite is taken. Data that is influenced by $CO_2$ is in bold.*

Next, 6 simulations are run to test the effect of chemically altering $\mu_s$, $\mu_d$, and cohesion on the amount, timing and magnitude of rupture events (simulations 2 to 7 in table 3). The conducted tests and input values are shown in table 3. As the spatiotemporal relationship between the $CO_2$ plume, cold front and pressure front are key ingredients affecting fault stability, all runs are repeated for a fault with the top at 500 m and 600 m from the injection well, which is approximately the location where the cold front ends using the parameters of this study. Linear relationships between saturation and cohesion or frictional strength are deducted from experimental studies or studies from natural $CO_2$ analogues as shown in text below.

Static friction is one of the factors suggested to be altered by the study of Rattez et al. (2021). In simulation 2 and 3, a 25 cm wide fault zone composed of pure calcite in a sandstone reservoir without any calcite is assumed. Simulating a pure calcite fault is chosen to mimic the pure calcite used in the study of Rattez et al. (2021). All aqueous $CO_2$ passing through the fault zone is modeled to react directly. Once $\mu_s$ is lowered by chemical alteration, i.e. by calcite dissolution, it remains at a lower value for the rest of the simulation. No reprecipitation of calcite is modeled in the simulation. Rattez et al. (2021) found both a decrease in both static friction (27.8%, 0.34 to 0.24) as residual friction (57.6%, 0.33 to 0.14) upon dissolving 25% of calcite mass from pure calcite. Based on the experimental results of Rattez et al., (2021), a linear decrease in static friction of 27.8% (0.5 to 0.36) is modeled due to a removal of 25% of the calcite (simulation 2). Next, a linear decrease of 57.6% (0.35 to 0.15) of dynamic friction is modeled upon removal of 25% of the calcite (simulation 3). Other values of calcite removal in mass percentage are interpolated/extrapolated linearly. Both results are tested in separate runs to compare the relative effect on rupture events.

Dynamic friction is found to either increase or diminish according to the study of Bakker (2017), depending on whether only calcite is leeched from the rock or whether reprecipitation of other minerals occurs. In the simulations 4 to 7, starting mineralogical compositions are taken from the study of Bakker (2017). Their starting material is a carbonate-bearing claystone containing ~25 mass-percent calcite. The fault is assumed to be composed of the same material as the whole rock. Upon complete leaching of the calcite from the rock, their study found dynamic friction to diminish from 0.35 to 0.27. Other results from their long-term geochemical modeling suggest that complete dissolution of calcite and reprecipitation of other minerals (mainly Kaolinite, $Al_2Si_2O_5(OH)_4$) could lead to an increase of dynamic friction from 0.35 to 0.40. Both effects are tested separately in simulations 4 and 5 respectively.

Cohesion is found to diminish from 14.5 to 10.5 MPa (27.6 % loss) upon removal of 4.5 mass-percent calcite from intact calcite-cemented sandstone cylinders by aqueous $CO_2$ in the study of (Lamy-Chappuis et al., 2016). The study of Hangx et al., 2015 found similar lowered cohesive strength potentially resultant from long term $CO_2$ influence from 22.7 to 16.8 (26.0% loss), yet no corresponding amount of calcite mass-percent loss was mentioned. These are, however, cohesion values for an unfractured rock. Previously faulted zones will remain somewhat weaker than their unfaulted protolith. Therefore, 2 cases are tested in which a starting cohesion of 1 MPa (simulation 6) and 10 MPa (simulation 7) is influenced as such that a 4.5 mass-percent calcite translates to a 25% reduction in cohesion. As mentioned before, once a patch has ruptured, cohesion is lost and remains at zero for the remainder of the simulation.

# Results

## TOUGH results, spatiotemporal relationship P, T and $CO_2$(aq)

The TOUGH2 ECO2M module is run for a total of 150 years, of which injection starts after 50 years. In the results section below, t=0 yrs. is taken at the start of the injection. The injection stops at t= 50 yrs. and the simulation stops at t = 100 yrs. TOUGH output is visualized in figure 7 and figure 8. The temperature and pressure development in the 50 years of injection and 50 years post-injection are visualized in figure 8. In the first 50 years, a clear development of a cold front of approximately the injection temperature of 20 °C is shown. The cold area spreads from the injection location outwards, also cooling parts of the caprock and under burden. After the injection is stopped, the overall temperature of the cold front gradually increases again. Using the reservoir properties of this study, the initial injection location will have returned to a temperature of ~ 35°C again 50 years after injection has stopped.

In the simulation either liquid $H_2O$, liquid $CO_2$, or aqueous $CO_2$ is present in the pore space. Figure 7 shows the development of the spatial distribution of aqueous $CO_2$ expressed in the mass percentage of the total pore fluid. Visualizing the mass-% of the aqueous $CO_2$ component is chosen because water acts as a conduit for the chemical changes that occur upon dissolving $CO_2$, and both the pure $H_2O$ and $CO_2$ phases are hardly reactive. The reservoir can broadly be split up into 4 zones, increasingly closer to the injection well: 1) A zone containing pure liquid $CO_2$ and residual immiscible pore water that got trapped by the liquid $CO_2$. 2) A zone in which the composition of the pore fluid gradually switches from liquid $CO_2$ to fully $CO_2$ saturated water. 3) a zone in which $CO_2$ is dissolved in the water phase, leading to a high mass fraction of $CO_2$ (aq). $CO_2$ concentration is highest near zone 2 where the water phase is fully saturated and $CO_2$ concentration decreases outwards from the injection well. 4) A zone containing pure water, no $CO_2$ influence noted. The highest concentration of aqueous $CO_2$, up to 0.06 mass%, is found in zones 2 and 3. In other words, zones 2 and 3 are where the pH of the pore fluid is most affected by dissolved $CO_2$ and thus most chemical effects are expected. Maximum dissolved $CO_2$ concentrations at the fault are found to be ~1.33 mol/kg water. A continuously increasing amount of aqueous $CO_2$, after the injection has stopped, can be observed as a result of the continuous mixing of the liquid $CO_2$ and $H_2O$ phase. An important result from the plots in figures 7 and 8 is the difference in spatial developments of P, T, and $CO_2$ (aq).

Figure 8 clearly shows the difference in the spatial extent of the temperature and pressure effect. The pressure is found to increase quite rapidly throughout the whole reservoir. Initially, a slight gradient is created, as in the bottom part of the reservoir pressure increases faster. Pore pressures are found to increase towards a final pore pressure of 31.5 MPa upon the 4 Mt/year injection rates during 50 years of injection and remain high during the rest of the simulation. It should be noted that the absolute numbers of pressure are highly dependent on the assumptions taken in this study regarding injection rate and reservoir properties like reservoir height, porosity/permeability, and spatial extent of the reservoir.

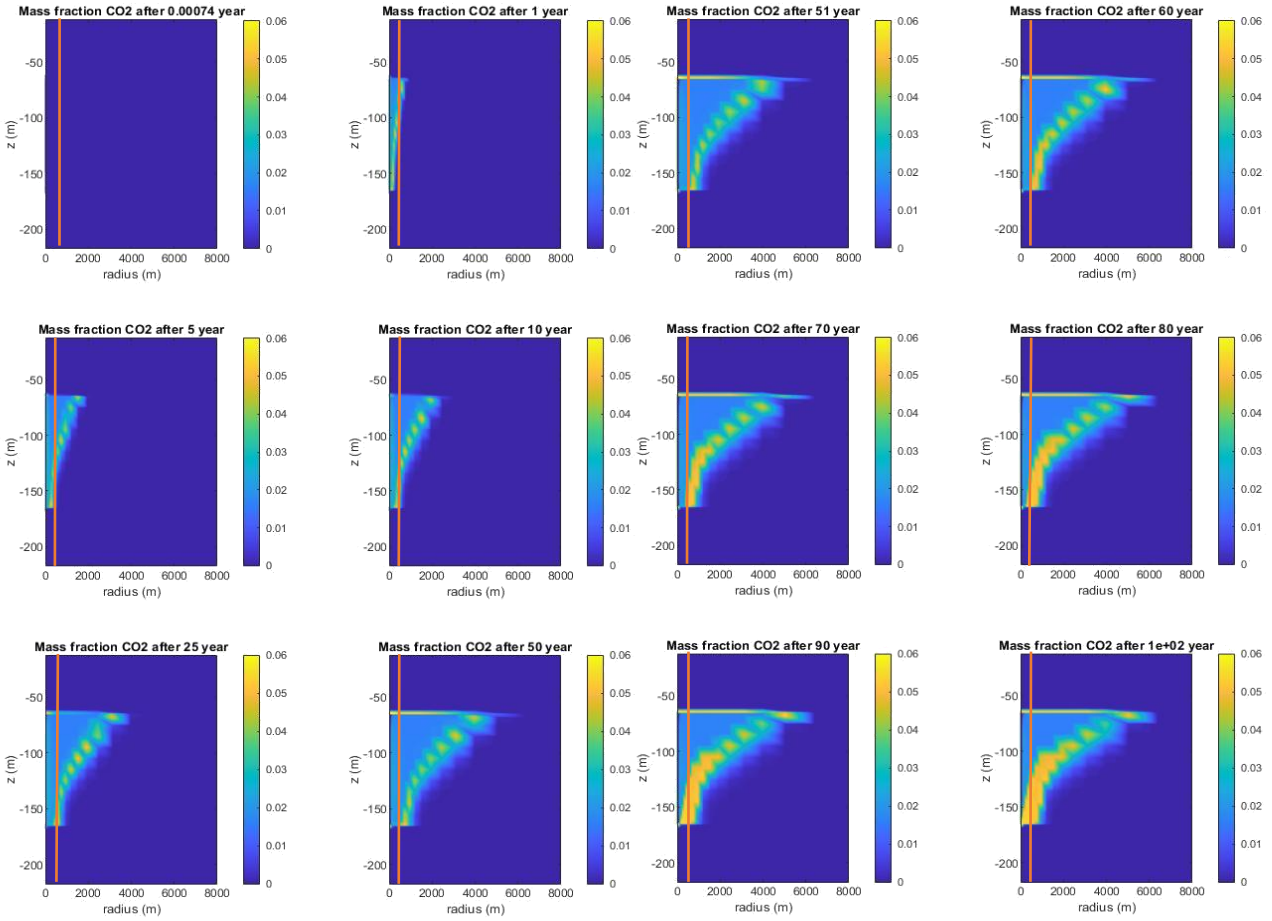


*Figure 8: Development of the $CO_2$ plume in the reservoir simulation. Left is plotted the values during injection of $CO_2$ at t = 0, 1, 5, 10, 25 and 50 years. On the right are plotted the values after the injection has stopped at t = 51, 60, 70, 80, 90 and 100 years. The aqueous $CO_2$ is expressed in mass % of the pore fluid. The location of the fault at 500 m is plotted in red*

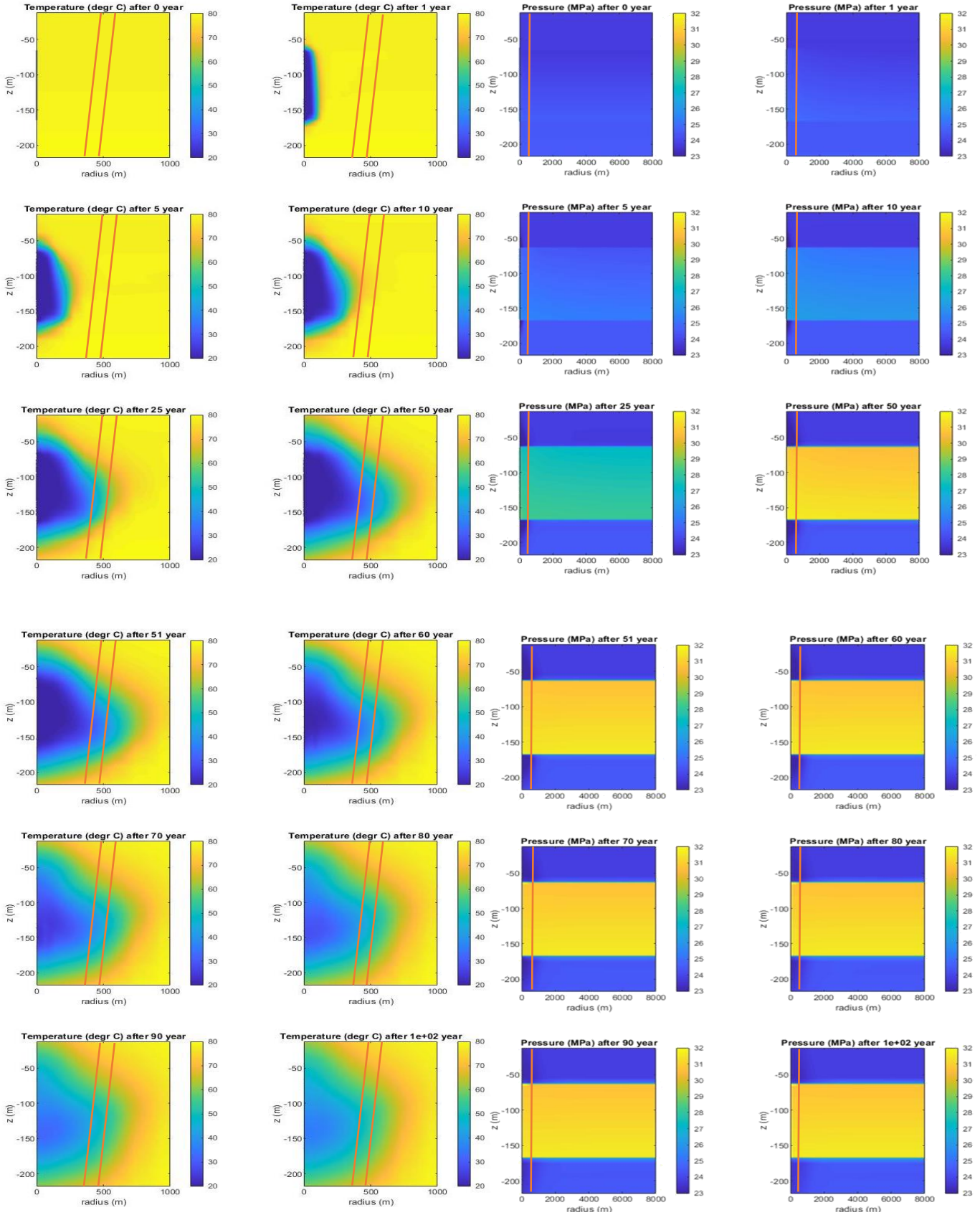


*Figure 8: Visualization of TOUGH flow simulation.* ***Left:*** *plots containing the temperature in the reservoir.* ***Right:*** *Plots showing the pressure development in the reservoir. Top part of the figure shows plots during injection at t = 0, 1, 5, 10, 25 and 50 years, bottom half shows plots post injection at t = 51, 60, 70, 80, 90 and 100 years. In all figures, the injection well is found at radius = 0, and radius is the distance with respect to the well. The top of the reservoir is found at z = -53m and bottom of the reservoir at -153m with respect to the top of the model. Actual modelled depth of the reservoir is between 2406 and 2506m. the location of the faults at 500 m and 600 m are shown in the temperature plots in red. Only the fault at 500m is plotted in the temperature plots.*

## SRIMA results, stress changes at fault surface

Effective stress calculations on the fault plane are output from SRIMA, plotted for the 500m fault in figure 9. The images show the development of the main stress directions over time during and after injection. Initially, stresses in all directions are high, 27-30 MPa (σ2 & σ3) and 52 to 58 MPa (σ1). Effective stresses gradually decrease, largely as a result of the increasing pore pressure in the reservoir, to values of 14-19 MPa (σ2 & σ3) and ~46-48 MPa (σ1) within the reservoir. In the plots of (σ2 & σ3), the development of the cold front and corresponding thermo-elastic stress reduction is visible. The center part of the fault (i.e., closest to the injection well) is influenced the most by the cold front, which is reflected in lower effective stresses there. After injection is stopped, stresses remain high. The concentric circles forming steps are an artifact from the way SRIMA calculates the thermos-elastic stresses but are not expected to influence further simulations significantly as the steps are relatively small.

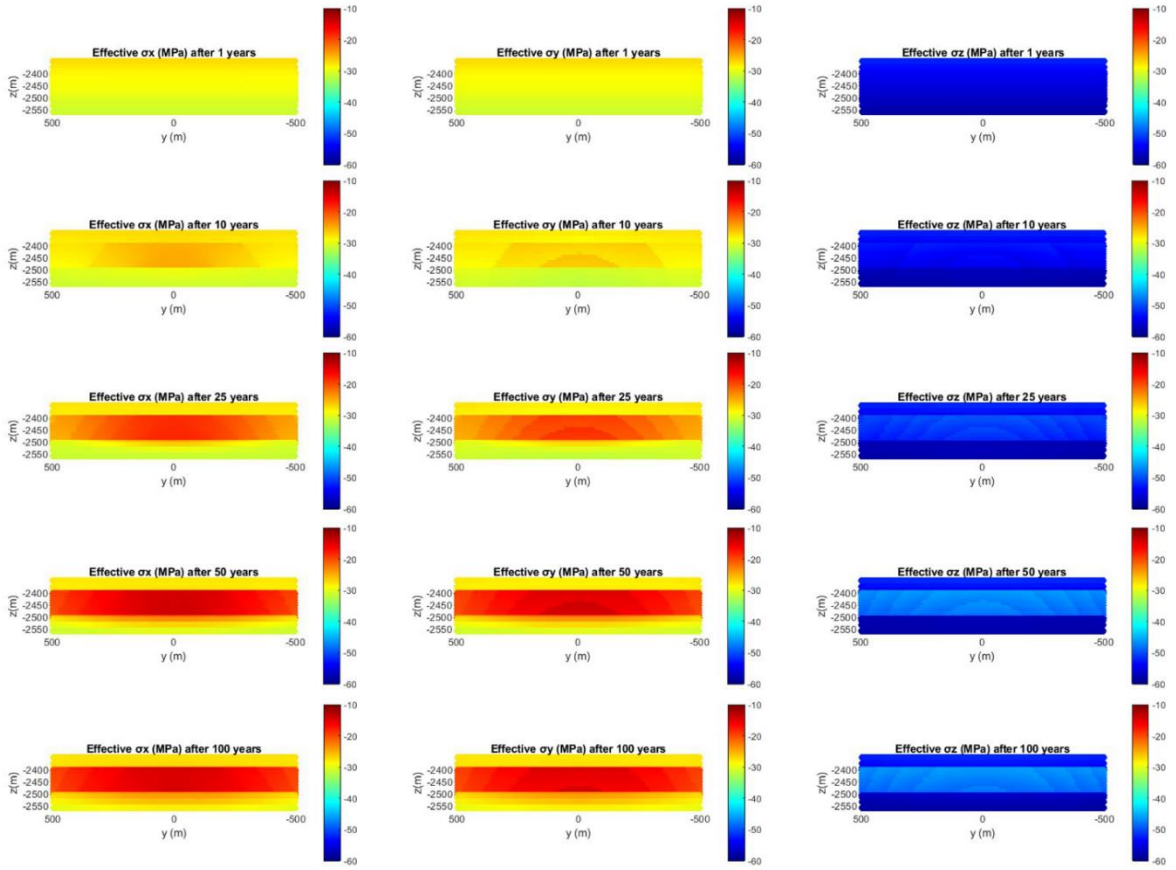


*Figure 9: Effective stress values found at the 500m fault for **left:** σx, **middle:** σy and **right:** σz. Stress values are plotted for t = 0, 10, 25, 50 and 100 years. Initially a gradual increase of stress is found with depth corresponding to a standard dz/dσ of ~32.4 KPA/m and horizontal/vertical stress ratio of 0.67. gradually stresses are increased throughout the reservoir as a result from changing pressure and temperatures. Stresses in the cap rock and under burden are also slightly affected.*

Similar plots are made for the temperature, pressure, and aqueous $CO_2$ mass fraction of the pore fluid (figure 10), also plotted for the 500m fault. Again, the clear difference in the spatial extent of the $CO_2$, temperature, and pore pressure effects can be observed. Another important observation to make is how time plays a key role, as temperature effects are shown not to influence the fault area much directly in the first 10 years of injection, whereas the front (the reactive zones 2 and 3) of the $CO_2$ plume has largely passed the fault after 10 years. The lowest temperature found at the fault surface is ~30°. The ellipse-shaped cold front is represented in the lowered effective stresses in figure 9, where slightly lower values of effective stress are found at the center of the fault. Also, the increase in temperature after t = 100 years (visible in figure 8) is represented as a slight increase in stress in figure 9. Pressure is found

to increase uniform over the fault surface within the reservoir bounds (figure 10). It is clear that pressure, temperature and $CO_2$ weakening effects affect the stability of faults following a different spatiotemporal pattern. The different spatiotemporal pattern largely affects the effective stress changes and affects the timing of ruptures and extent of the ruptured area, as will be further described in the discussion.

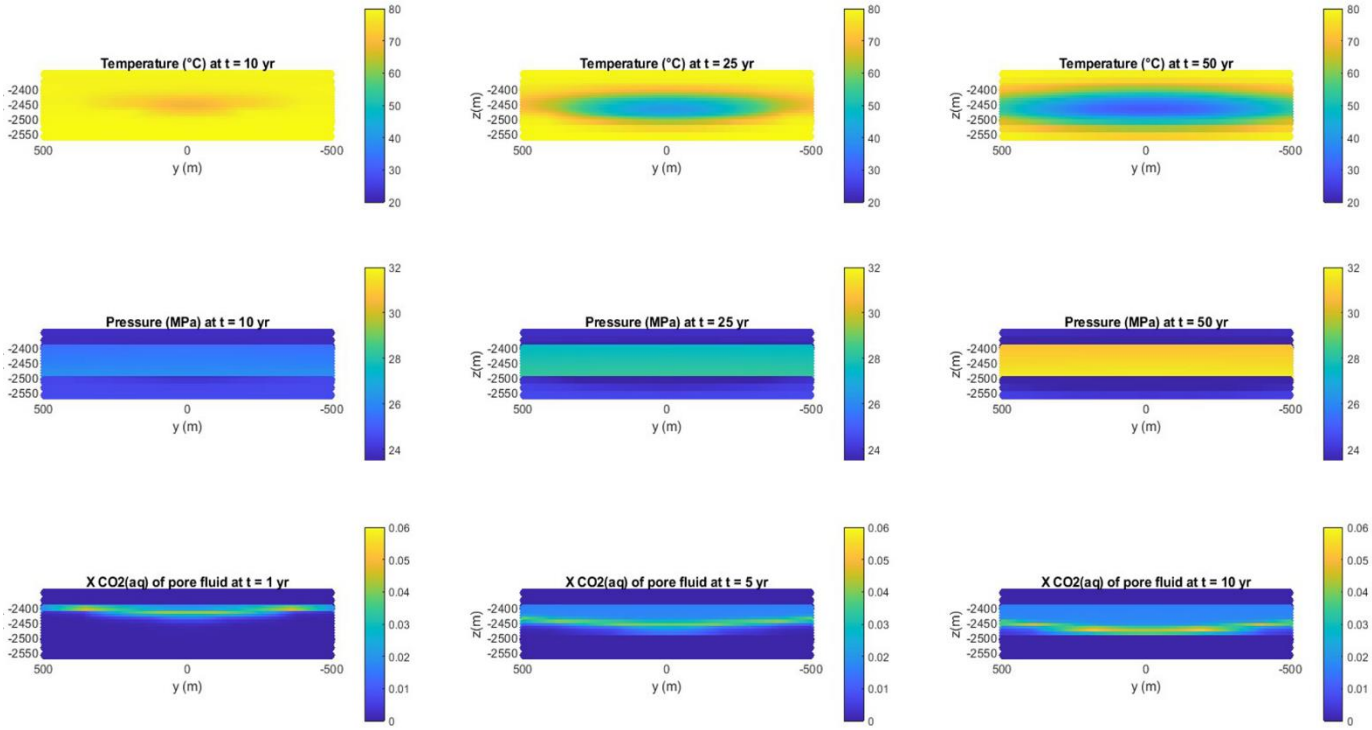


*Figure 10: Plots of **top:** temperature, **middle:** Pressure and **bottom:** XCO2(aq) of the pore fluid. Temperature and pressure are plotted at t = 10, 25 and 50 yrs. This shows the gradual development of an ellipse shaped cold front reaching the fault surface. Also shown is the gradual increase of pressure throughout the reservoir. This increase of pressure is found to be uniformly over the fault surface. XCO2(aq) of pore fluid is plotted at t = 1, 5, and 10 years. Clearly shown is how a region of enhanced CO2(aq) spreads throughout the reservoir (corresponding to zone 2 and 3 in text), followed by a lowered amount of CO2(aq) present in the residual water content in the rock. Also clearly visualized is the difference in spatial effect of the three plotted variables*

## BSQuakeSim results, rupture simulations

### Fault at 500 m, within cold front

An initial test is performed to determine whether criticality is reached on the fault surface without any chemical influence, and what the seismicity and slip along the surface look like in the base case (simulation 1). BSQuakeSim results are expressed in plots containing the total slip distance along the fault area and plots combining the magnitude and timing of rupture events in figure 12 and 14.

Figure 11 shows the effective normal stress and effective shear stress within the reservoir at the timing of initial criticality. Effective normal stresses are lowered in the reservoir mainly resultant from the pore pressure increase. Shear stress is increased mainly as a result of the thermo-elastic stresses. Block-Spring combines the static friction, cohesion, effective normal stress, and effective shear stress to determine criticality according to the Mohr coulomb failure criterion (equation 4). Figure 11 shows the spatial extent of the reaction front and its effect on static friction, dynamic friction, and cohesion. Visible is that both at initial criticality as at final timestep, $CO_2$ interaction has either lowered or increased the different parameters for most of the reservoir, but not within the under burden or cap rock, as expected from the low permeability there.

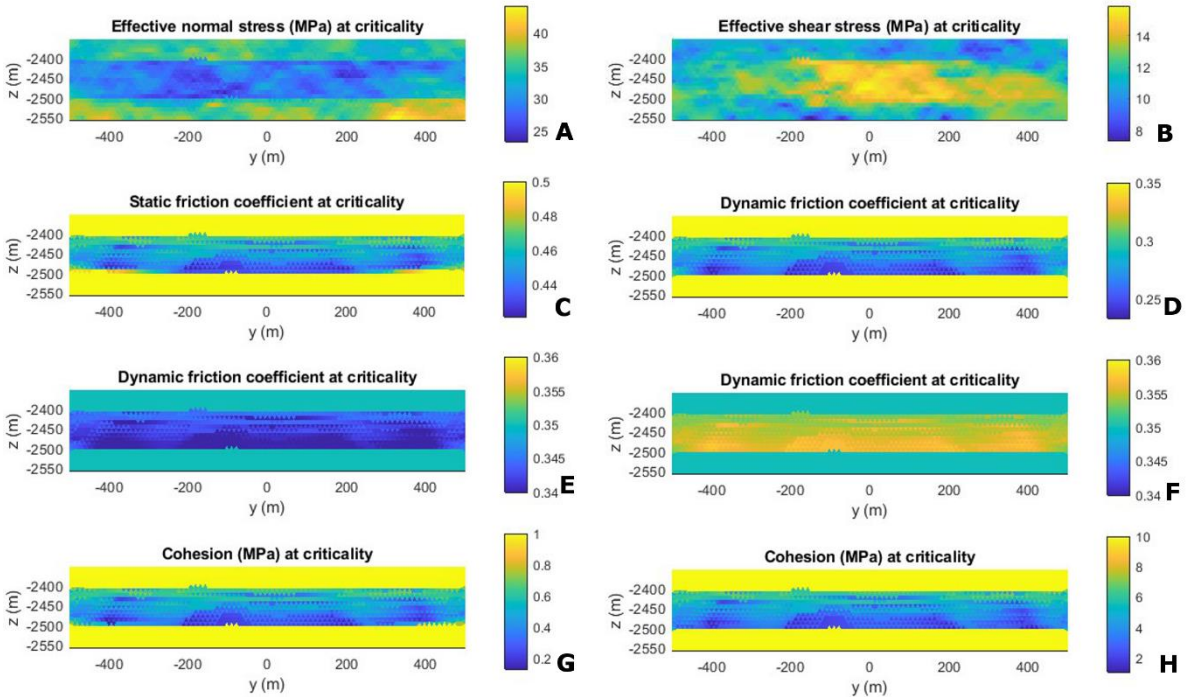


*Figure 11: Values of various parameters at criticality for : **A)** simulation 1, **B)** simulation 1, **C)** simulation 2, **D)** simulation 3. **E)** simulation 4, **F)** simulation 5, **G)** simulation 6 and **H)** simulation 7.*

Figure 12 contains the results of simulations 1 to 7, corresponding to the set-ups shown in table 3. The top plots show the results of the base case run, in which no $CO_2$ effect was tested. The slip figure shows that most of the slip along the fault has occurred in the central part of the fault, which is approximately where the temperature front of the cool $CO_2$ hits the fault surface. Maximum slip at any location was measured to be 0.024 m accommodated over a total of 281 individual rupture events. The figure on the right shows that seismicity started at 27.44 years. There is a clear line of minimum seismic event magnitude visible with a moment magnitude of -2 representing the energy that is released from a small slip distance along a single triangular patch, which does not trigger any other patches. The amount and severity of seismic events drop gradually after injection seizes at t = 50 years. In total 2 rupture events are simulated with Mw>1.0. No ruptures are modeled to be Mw>3.0.

Results from simulation 2 (figure 12) show a clear increase in the total amount of slip along the surface, the number of rupture events, and the severity of the rupture event. 10 rupture events are noted with a moment magnitude of Mw>1. Rupture events start at a timing of t= 16.9 years after injection started. $CO_2$ has thus affected frictional strength before that timing, as is shown in figure 11. A maximum slip of 0.0249 m was achieved after a total of 675 individual rupture events.

Simulation 3 shows a clear increase in total rupture area, total slip distance, and a decrease in the total amount of rupture events when compared to the base case (simulation 1). 2 rupture events of Mw> 3.0 were noted, which resulted in more slip than simulations 1 and 2. A maximum slip of 0.0361 m was created over 126 individual rupture events. Similar relationships as between simulations 1 and 3 were found between simulation 1, 4, and 5, in which changes in the dynamic friction rather than the static friction were tested. Figure 11 shows the minimum and maximum value of $\mu_d$ reached at initial criticality at the fault surface in simulations 4 and 5 respectively. The figure shows how applying a different relationship between $CO_2$ concentration and dynamic friction leads to either enhanced or diminished values of dynamic friction in the reservoir. The plots of simulation 4 show initiation of rupture events at t = 27.44 years and equal to the timing of the first rupture events of simulation 1 (figure 12). The model shows an increased total slip distance and total slip area when compared to simulation 1. A maximum slip of 0.0280 m was accommodated in 178 individual rupture events. Simulation 5 shows the initiation of rupture events at similar timing as simulations 1 and 4. The model shows a

decreased total slip distance and slip area. A maximum slip of 0.0242 m was accommodated in 170 individual rupture events. Both simulations 4 as 5 show a decrease in rupture events upon changing the dynamic friction.

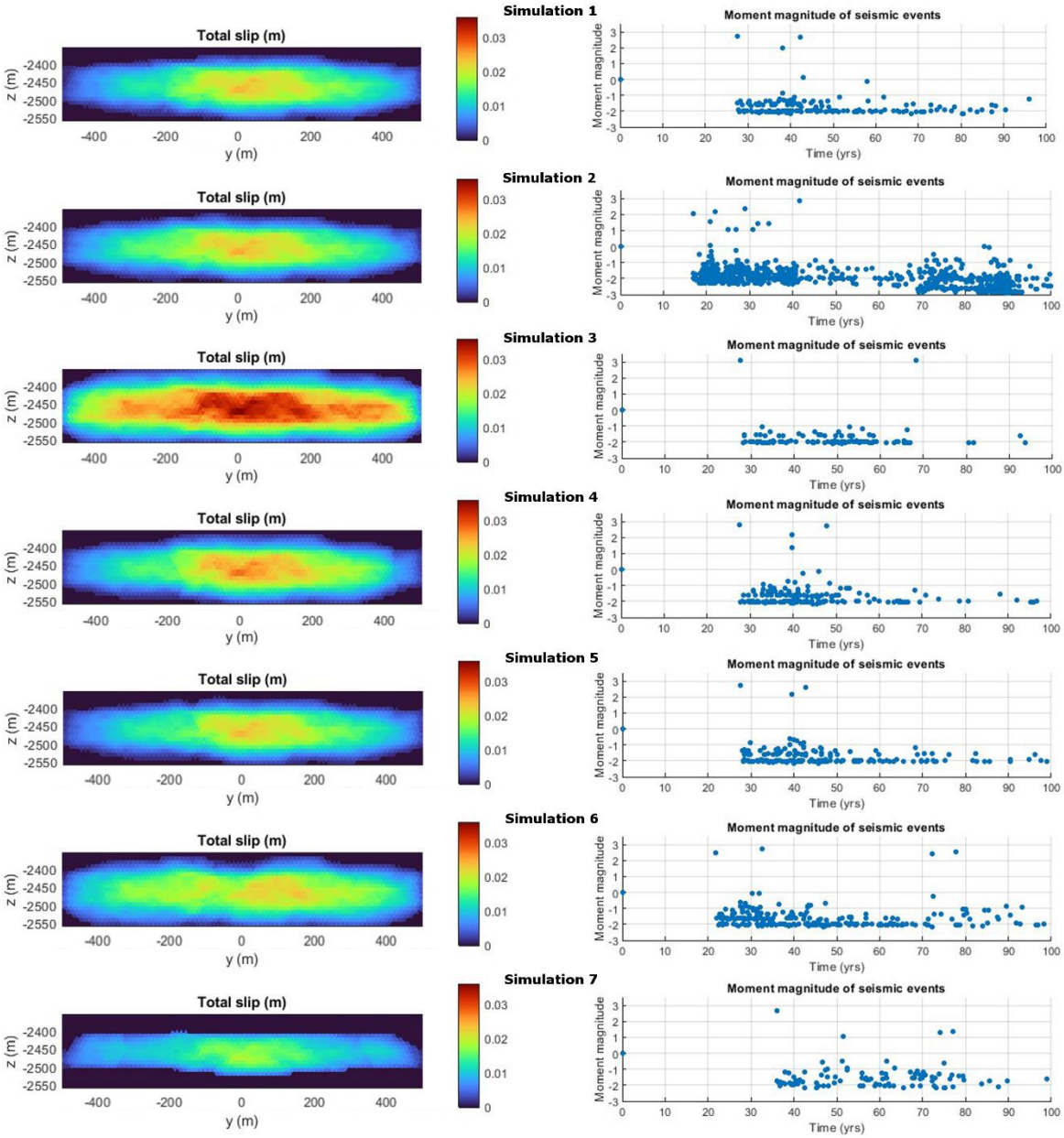


*Figure 12: Plot showing the output of Block-spring simulations 1 to 7 for a fault for which the top is located at 500 m from the injection well and dipping 60° in the direction of the well.* ***Left:*** *Plots showing the total slip (m) along the fault surface at any triangular patch during the full simulation.* ***Right:*** *plots showing the moment magnitude (in Mw) of each rupture event plotted against time (s). Constant color values and axis limits are used for all plots. See table 3 and text for details about the different simulation.*

Figure 12 also shows the cohesion values at the fault surface at the point of initial criticality in simulation 6. Cohesion values of simulation 7 are similar to these values but multiplied by a factor of 10x. Most of the cohesion in the reservoir has already been lost due to chemical alteration before the first rupture events. Simulations 6 and 7 show that changing cohesion has a large effect on the rupture events during the simulations (figure 12). In both cases, cohesion was linked to $CO_2$ (aq) such that 4.5 mass % loss of rock material in the form of calcite corresponds to a 25% lowered value for cohesion. As a result, at some locations along the fault plane fault cohesion nearly completely reacted away before

the first rupture events. Less cohesion results in a smaller amount of stress buildup compared to the base case, and therefore rupture events commence at t = 22.8 years in simulation 6.

Compared to the base case, simulation 6 shows a larger number of rupture events with Mw>1. The simulation shows slightly fewer total individual rupture events (260) accommodating a total maximum slip of 0.0236 m. The lower amount of slip is the result of less stress buildup on individual patches. The total area of patches that have slipped is increased in simulation 6 with respect to simulation one as a result of the lowered strength of individual patches. The rupture area extends also outside of the reservoir. In the current setup of the model, rupture events will also occur within under burden or cap rock. Released energy from slipping patches within the reservoir has the potential to trigger slip of patches outside of the reservoir. It should be noted that no different value of fault strength/cohesion is used in the caprock or under burden in the current workflow. In simulation 7 the cohesion at the start of the simulation is taken at 10 MPa, which is 10 times the cohesion of simulation 6. However, fewer rupture events, and a decreased slipped area are found. Slip is contained within the boundaries of the reservoir, as cohesion values are not lowered in the caprock/under burden since little $CO_2$ is expected to be present there (see figure 11). Rupture events will commence later, as a higher buildup of stress is required to overcome the critical state. $CO_2$ interaction have not lowered cohesion as such that the values of cohesion in simulation 7 become lower than those of the base case.

### Fault at 600 m, just outside cold front

As described previously, differences in the spatial extent of pressure, temperature, and CO2 concentration were found in reservoir simulations. All simulations described above were repeated for a fault at 600 m. At increased distance from the injection well, values for pressure and $CO_2$ concentrations are found to be nearly equal to those at a more proximal fault (see figures 7 and 8). The main difference is found in temperature, as at the distal m from the injection well, the end of the cold front is reached (see figure 8). The minimum temperature reached at the distal fault is 38.8°C at t = 50 years. Figure 13 shows the effective normal and shear stress and static friction at the fault surface when initial criticality is reached in simulation 2. The figure is nearly identical to figure 11 describing simulation 2 at the more proximal fault. The main difference is in the timing initial criticality: after 16.9 years for the proximal fault or after 28.7 years for the distal fault.

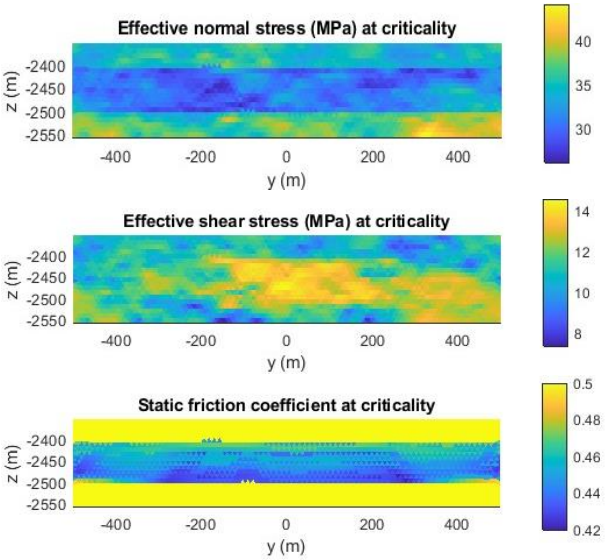


*Figure 13: Values of Effective normal stress, Shear stress and $\mu_s$ (static friction) as calculated by BSQuakeSim at initial criticality during simulation 2, fault at 600 m. Figure is nearly identical to figure 11 except for the spatial location of the fault and the timing of criticality (t = 28.7 years rather than t =16.9 years)*

Figure 14 shows the results for a dataset of runs identical to those described earlier, except for the absolute distance between the well and the fault (top of fault at 600 m versus 500 m). Figure 14 further shows that for all simulations, significantly fewer rupture events and less total slip is expected than in their equivalent run on a proximal fault.

The simulation shows that lowering $\mu_s$ (simulation 2) leads to a smaller amount of required buildup of stress, therefore seismicity will commence earlier during the simulation. The total amount of slip, however, is found to be less in the simulation. Lowering $\mu_s$ also leads to a lowered stress drop once criticality is reached, therefore less slip distance along the fault surface: a maximum total slip of 0.0165m accommodated in 340 individual rupture events. Changing $\mu_d$ (simulation 3) in the models

does not affect the initial criticality. Again $\mu_d$ is lowered, and the stress drop upon switching from static to dynamic friction becomes higher. More slip distance along patches occurs, and more long-range stress to be released on the rest of the fault surface. Ultimately lowering $\mu_d$ will result in a higher moment magnitude rupture event and a higher total amount of slip: a maximum total slip of 0.0287m accommodated in 3 individual rupture events for simulation 2. Almost all slip in simulation 3 results from a Mw 3.19 rupture event, which is the highest noted magnitude in all simulations in this study. The difference between simulations 1, 4, and 5 is limited.

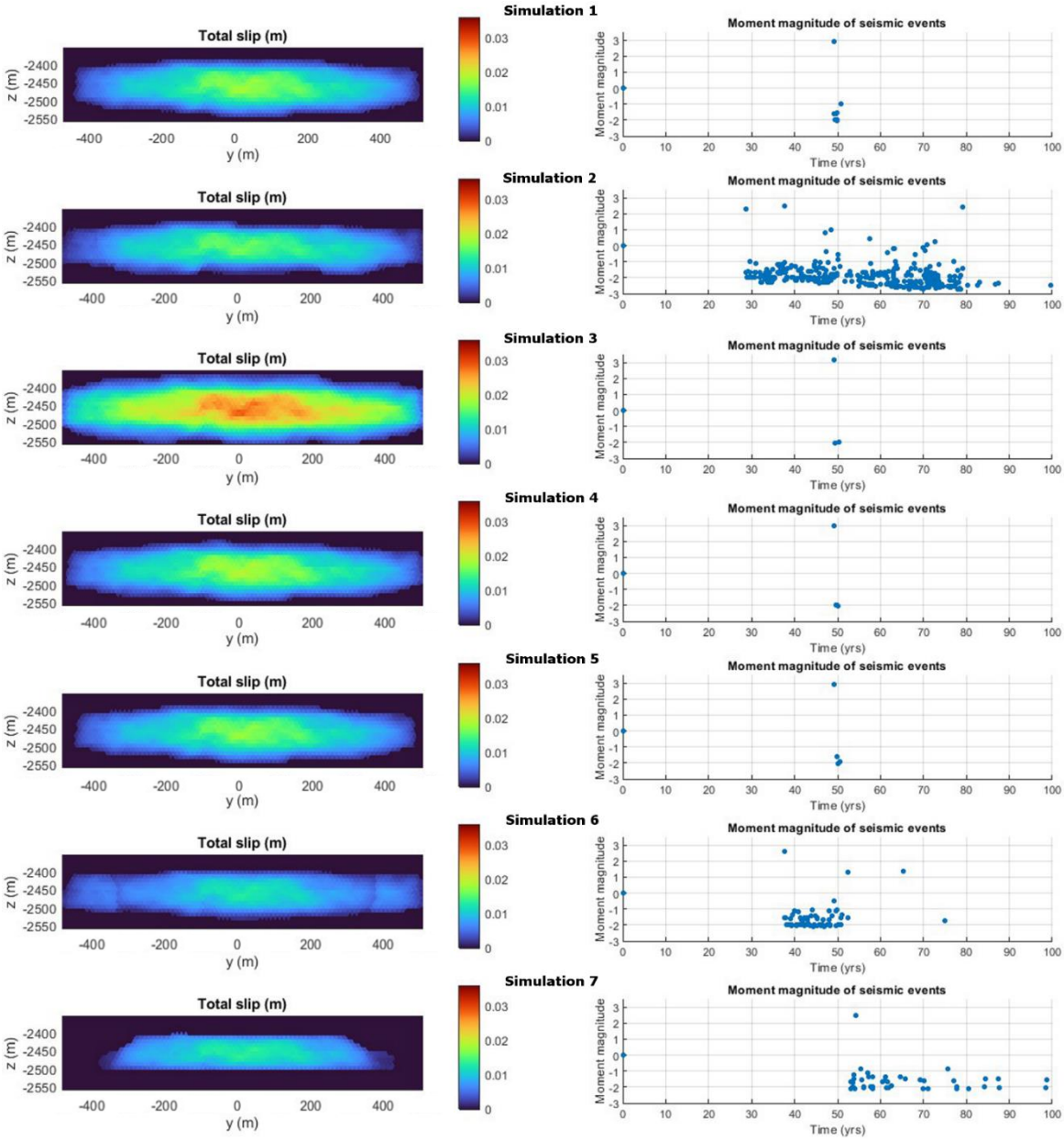


*Figure 14: Plot showing the output of Block-spring simulations 1 to 7 on a fault for which the top is located at 600 m from the injection well.* ***Left:*** *Plots showing the total slip (m) along the fault surface at any triangular patch during the full simulation.* ***Right:*** *plots showing the moment magnitude (in Mw) of each rupture event plotted against time (s). Constant color values and axis limits are used for all plots. See table 3 and text for details about the different simulation.*

Similar results are found for linking cohesion values to the $CO_2$ concentration at proximal and distal faults. If cohesion has been removed by reaction, less stress buildup is required to reach criticality. However, more rupture events are found in the simulation than compared to the base case. The

maximum of the total amount of slip along the fault surface is found to be less. Decreasing or increasing initial cohesion values also influences the timing of commencing of rupture events. In simulation 7, ruptures start after 53.14 years. Maximum stresses are reached at t =50 years when the injection is stopped and gradually declines afterwards. Therefore, after t=50 years, the chemical lowering of cohesion must have lowered the rock strength to allow the coulomb failure criterion to be reached.

The largest single rupture event noted in the simulations (simulation 3 of the distal fault, moment magnitude = 3.19Mw) slip occurred on 2628 of the 3122 patches, with an average slip of 0.01283 m per slipping patch. Slip during this rupture event occurred on an area of 202500 m2 of the total 240639 m2 fault surface modelled, which is 84.1 % of the total fault area in the region. A magnitude 1.35 Mw event in simulation 5 (increased stress drop) of the proximal fault corresponded to an area of 15535$m^2$, roughly the size of a 125 by 125 m fault. Similarly, a magnitude 1.53 Mw event in simulation 2 (decreased stress drop) corresponds to a rupture area of 25165$m^2$, roughly 159 x 159 m fault surface. Rupture events which only caused slip on 1 or 2 patches are found in the order of -2 Mw in most simulations, or less in simulation 2 where the stress drop on a single patch is progressively lowered by chemical alteration.

# Discussion

## Temperature, Pressure, and Saturation

It is evident from the ellipse-shaped pattern of fault slip shown in figures 12 and 14 that slip is most likely to commence in the center part (i.e. the part closest to the well) of the reservoir for all simulations in this study. Effective stress changes in SRIMA are calculated by adding the initial stresses, poro-elastic stresses from pressure changes, and thermo-elastic stresses from temperature changes and are visualised in figure 9. A clear decrease of effective main stresses througout the entire reservoir is the reflection of pore pressure increase. The slight decrease of effective main stresses in the middle of the fault area is the reflection of thermo-elastic stress lowering. Once the cold front reaches the fault an ellipse-shaped cooled area on the fault surface is created (as shown in figure 10). Such ellipse shape is not clearly shown in the change of main effective stresses (figure 9). When observing the effective normal stress and shear stress, an uniform decrease of normal stress throughout the entire reservoir is seen, corresponding to the pore pressure increase. An increase of shear stress is mainly found at the center part of the fault clostest to injection (i.e. y = 0 ), corresponding to the location of the cold front. Both poro-elastic as thermo-elastic effects are therefore found to contribute significantly to fault instability in the current simulation setup. The temperature effects are found to be the trigger of the rupture events in the current simulations, as is shown by the difference in seismicity between 500 m – 600 m and the absence of seismicity at 650 m. The triggering of rupture however requires an initial pore pressure increase to reach a state near criticality, which is also reflected in the fact that no rupture events would occur upon injection rates of 1 or 2 Mt/y. It thus largely depends on the selected reservoir properties, injection rate and injection temperature whether thermo-elastic or poro-elastic stresses contribute most to fault instability.

In the current setup, it is assumed that $CO_2$ reactions are found to lower the required effective stress change to trigger rupture events but the reactions do not create stress changes. Saturation of $CO_2$ spreads on a different spatiotemporal relationship along the fault surface than pressure or temperature, initially affecting the top part of the fault surface quite rapidly after injection starts, and slowly spreading also downwards along the fault surface. Most of the fault has experienced a high level of $CO_2$ alteration prior to the temperature front arriving at the fault's center (see figure 11, 13). As $CO_2$ reactions are found to predate the arrival of the cold front at the fault and triggering of ruptures along the faults, and do not cause stress changes, $CO_2$ reactions are not considered to be the main trigger of seismicity. However, they can significantly lower the required effective stress changes, in other words temperature changes, to trigger seismicity. One exception is simulation 6 for the fault at 600 m, where the fault

rupture is triggered at t = 53.14 years, 3.14 years after peak stresses are reached. Here loss of cohesion resultant from chemical reactions is found to be the triggering mechanism.

## $\mu_s$, $\mu_d$, and Cohesion

Lowering values of $\mu_s$ does lead to more rupture events, yet not always to larger total slip or moment magnitude (see fig 12 and 14). Lowering $\mu_s$ leads to triggering of events at higher effective normal stresses, as lower static friction coefficients lead to less fault strength. However, as $\mu_s$ switches to $\mu_d$ upon slip initiation, changing $\mu_s$ will only partly determine the slip along a patch. The amount of slip along a certain patch is calculated using the stress drop, which is the difference between shear strength on the patch before and after slip initiation (see figure 6). The released long-range stress on other patches upon the slip of a single patch is linear with the stress drop on that single patch. So, lowering $\mu_s$ values, while $\mu_d$ values are kept the same, leads to a smaller stress drop, less slip along a single patch, and therefore less released long-range stress on other patches. Chemically lowering the $\mu_s$ that triggers rupture events thus cause rupture events of lower total slip distance per patch and total lower energy release. Lowering $\mu s$ can however also positively affect the total slipped area in a single rupture, as the required stress for triggering slip on a single patch is lowered. Ultimately, the moment magnitude of a rupture event is calculated from the shear modulus, total slipped area and the mean slipped distance per patch within a single rupture event in Block-Spring. The maximum rupture moment magnitude is found less, resultant from the lowered $\mu_s$ value, which could be a desirable effect. On the contrary, the increase of rupture events is an undesirable effect if rupture events are of a magnitude that can be felt at the surface (further discussed below).

Changing the value of $\mu_d$ will mainly affect the stress drop upon rupture, and therefore the slip distance per slipping patch. As changing $\mu_d$ does not affect the Mohr Coulomb failure criterion, the required stress build-up to initiate the first rupture event will not be influenced. Lowering the value of $\mu_d$ leads to a higher stress drop upon rupture, therefore larger long-range stress release on the rest of the patches. Also, the final stress on the fault after the rupture event is controlled by the value of $\mu_d$, which is reflected by the switch from equation (4) to (5) upon rupture initiation. Therefore, the value of $\mu_d$ will influence the timing until the next event can occur. The higher stress drop on a patch results in larger magnitude rupture events than when compared to the base scenario (figures 12 and 14). In short, lowering $\mu_d$ causes higher magnitude seismicity with a lower frequency. It however does not affect the timing of the first rupture event, it only increases the magnitude. As high magnitude seismicity can be problematic, chemically lowering $\mu_d$ is found to be an undesirable effect of $CO_2$ injection.

In the study of Rattez et al. (2021) found peak friction (static friction) values in the order of 0.23 to 0.35 for pure calcite gouge, and dynamic friction values of 0.14 to 0.33. In this study, starting values in simulations of 0.5 for static friction, 0.35 for dynamic friction were used based on the frictional experiments of Bakker (2017). The percentile increase/decrease of $\mu_s$ or $\mu_d$ upon certain removal of calcite are taken from Rattez et al. (2021) or Bakker (2017). Their values led to final values of $0.35 < \mu_s < 0.5$ and $0.27 < \mu_d < 0.40$ in this study. These values are arguably low, when compared to values found in slide hold slide experiments performed on calcite faults (Chen et al., 2015). steady state friction coefficients were found in the order of 0.63 to 0.70 by the study of Chen et al. (2015). In wet experiments, the steady-state friction coefficient was found to increase even further after periods of hold, during which healing of fault gouge by compaction, pressure solution led to further enhancing friction coefficients. Such higher values would have implications on the stress buildup, stress drop, and rupture size as argued in text above. It is beyond the scope of this study to establish accurate absolute values of $\mu_s$ and $\mu_d$. It could be argued that the absolute starting values of both $\mu_s$ and $\mu_d$ used in this study are on the low side. The absolute values of the parameters, however, do not influence the relative effect of changing $\mu_s$ and $\mu_d$ on seismicity shown in text above.

Changing the starting cohesion solely affects the required stress build-up to initiate the first rupture event on individual patches, as is shown in the difference in timing of first rupture events between

simulations 6 and 7 (figures 12 and 14). Increasing cohesion will result in a higher build-up of stress to reach criticality at a first rupture event. The high initial stress drop will result in a high moment magnitude event, slip on a large area of the fault plane and therefore cause cohesion to be lost (i.e., cohesion values are turned to "0") in a large area of the fault. As cohesion values are assumed to remain "0" in this study, rupture events afterwards will be of lower moment magnitude. A higher value of cohesion results in higher moment magnitude rupture events, at least for the first rupture event, which is an undesirable effect. On the contrary, a high initial cohesion value can prevent that criticality is reached at all.

Chemically lowering cohesion values leads to less stress required to reach criticality. As stress is built up gradually in the simulations in this study, the timing of the first rupture events is affected (simulation 1 versus 6). As the stress drop is lowered, rupture events of lower moment magnitude are found in this study. However, as fault strength is lowered in most of the reservoir, the lower stress drop still causes a large area within the reservoir to slip, but only for less distance. Chemically lowering the cohesion is undesirable if no rupture events are permitted. If low magnitude rupture events are permitted, chemically lowering cohesion could be interesting as less magnitude is expected.

In current literature, cohesion and static friction are often combined into a single parameter called "friction" or "apparent friction". However, as shown in text above, alteration of the 2 leads to different results regarding rupture area size, frequency and magnitude. Therefore, weakening of static friction and cohesion should be studied separately in the context of rupture activation potential in CCS projects. The relative contribution of both parameters strongly depends on the normal stress that is present on the fault surface, as can be deducted from the Mohr coulomb failure criterion: $\tau_s = \mu_s \sigma_n + S_0$ in which the contribution of static friction to shear strength is linked to the effective normal stress. The answer to the question whether removal of cohesion or static friction leads to the highest magnitude rupture events depends largely on the pressure related parameters (i.e., injection rate, pore pressure) and absolute values of $\mu_s$ and $S_0$.

## Comparison to other studies

The main mechanisms affecting fault stability and triggering seismicity related to $CO_2$ injection are (stated by Vilarrasa et al. (2019): 1) Stress state changes in response to pore pressure variations. 2) Thermo-elastic effects from cold $CO_2$ injection 3) Stress changes arising from contrasts in rock properties between geological layers 4) Stress redistribution around a portion of a fracture that undergoes shear slip. 5) Aseismic slip contributions to the overall stress state. 6) Geochemical reactions altering frictional strength. 7) Heterogeneity in rock type, fault strength and the stress field. In the workflow in this study, all parameters are taken in account when considering fault reactivation except for mechanisms "5" and "7". Long-range stress contribution slipped fault regions are added to the overall stress state of the system, but whether slip is seismic or aseismic not taken in account. The role of aseismic slip is further discussed below. Also, the heterogeneity of fault strength will be discussed further below.

The flow modelling of Vilarrasa et al., (2019) found highly similar spatiotemporal relationships for the pore pressure increase, temperature decrease and $CO_2$ saturation. In their modelling, 0,2 mt/yrs. is injected in a 20 m thick reservoir at a temperature of 20 °C. According to them, cooling of the reservoir mainly advances by advection, but also extends in the lower portion of the caprock by conduction. As the temperature-induced stresses are not isotropic (see figure 9), fracture stability depends on the stress regime: normal faulting, strike slip or reverse (Vilarrasa, 2016). In regions experiencing cooling, the thermal stress reduction in the minimum horizontal stress is larger than the stress reduction in vertical stress, similar to findings in this study (figure 9), which triggers instability (Vilarrasa, 2016). The thermal compromising of fault stability is reflected in the findings of this study that temperature is found to be the triggering mechanism for fault instability once pressure increase has brought faults in a near critical state. The modelling of Vilarrasa et al., (2019) shows little temperature decrease in the caprock,

therefore fracture stability is more compromised in the reservoir than in the caprock. Seismicity in the reservoir is triggered in their study, which could enhance permeability and thus could be desired, while maintaining the caprock sealing capacity. In this study, temperature effects are found to affect the cap rock quite far. Also, the area included in rupture events in this study spans far outside of the reservoir into the cap rock, potentially compromising sealing capacity of the caprock. Accepting small scale seismicity to enhance permeability, as suggested by (Vilarrasa et al., 2013) should therefore be treated with care.

In this study, instantaneous dissolving calcite is assumed. Also is assumed that the chemical reactions occurring are similar along each part of the fault, and that the fault is equally porous to the reservoir. These assumptions are thought to largely affect the way the fault weakens. In natural analogues, it is found that the heterogeneity of the rock material influences the way the material is chemically altered (Hangx et al., 2015). If dissolution of the calcite material and precipitation of other minerals occurs non-uniform over the fault zone, relatively porous weaker zones and cemented stronger zones can be created (Hangx et al., 2015). In their study, $CO_2$-exposed, highly porous zones showed approximately 1/3rd lower uniaxial compressive strength values, lower values of coefficient of friction ($\mu = 0.82$ versus $\mu = 1.02$), and lowered values of cohesion ($S_0 = 16.8$ versus $S_0 = 22.7$) upon dissolution of anhydrite. A friction coefficient reduction of 20% and cohesion reduction of 26% are comparable to the percentile reduction of both in this study. Their study found that overall, $CO_2$-exposure did not lead to drastic mineralogical changes in most of the rock. In other words, the homogeneous weakening of the rock, as is occurring in this study, is found unlikely by the study of Hangx et al. (2015). However, their study however stated that for certain rock conditions regarding high porosity, permeability, as is the case in this study, rock strength can certainly be lowered significantly by $CO_2$-exposure.

Such localized porous zone, and localized weakening of patches of the fault can result in heterogeneity of fault strength, and in different ratios of calcite-quartz or calcite-clay-quartz. Laboratory friction experiments from Bedford et al., (2022) have shown that such fault heterogeneity will result in an overall weakening of the fault strength resulting from differential compaction of different material, shear localization and stress concentration on stronger patches and, when present, the smearing of clay. Their study also found that heterogeneity of the fault gouge affects whether aseismic or seismic slip is expected, which affects the moment magnitude of rupture events. Whether localized weakening of fault rock occurs depends on overall grain reactivity, porosity, but also overall versus local porosity, and cement content and distribution as shown for anhydrite in figure 15 (Hangx et al., 2015). If calcite cement is part of the supporting framework of the rock, which depends on the depositional environment of the sediments, dissolution of cement will have likely significant effects. In the case of a calcite cemented fault gouge, like in the simulations in this study, all 3 cases in figure 15 are possible and therefore can not be fully ruled out. In this study, the artificial roughness assigned to the fault surface results in a heterogeneous fault strenght. However, the chemical weakening of the fault is not heterogeneous. Therefore, when modeling $CO_2$ injeciton in a realistic way, heterogeneity in fault weakening or fault material should be accounted for.

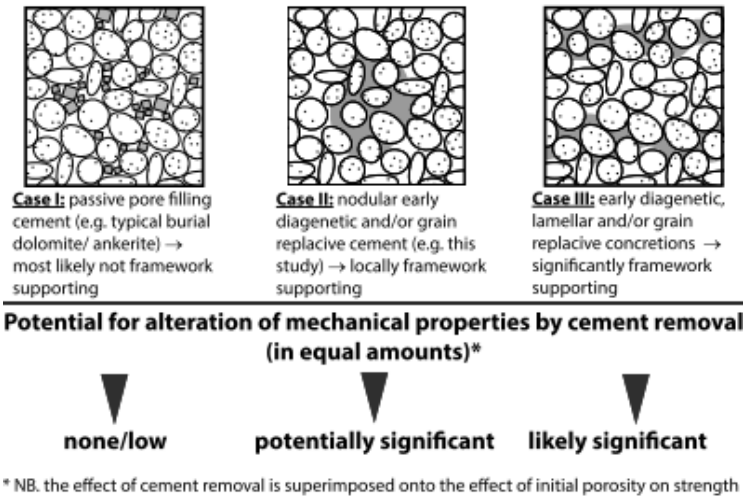


*Figure 15: different cases of cement types in granular materials like sandstone and the significance of alteration of mechanical properties by anhydrite cement removal. Figure taken from (Hangx et al., 2015).*

Triggering of seismicity was mostly deducted to temperature changes in this study, however a decrease of cohesion or static friction coefficient was also found to be a potential trigger for seismicity. Long-term alteration and correlated weakening of faults by circulating $CO_2$ saturated water has been suggested to be the trigger for earthquake swarms in West Bohemia, Czech Republic ((Heinicke et al., 2009; Vavryčuk & Hrubcová, 2017). Their studies examined the full seismic moment tensors of a swarm of microearthquakes in West Bohemia. Fracturing at the start of the swarm was not initiated by fluid flow, and not by redistribution of Coulomb stress. The seismic swarm can only be explained by a fault weakening model (see figure 16) proposed by (Vavryčuk & Hrubcová, 2017), in which fault degradation due to long-lasting chemical an hydrothermal, fluid-rock interactions in $CO_2$ saturated fluids occurs. Their study proposed the porosity of the fault gouge to increase, weakening the frictional strength of the fault, which in their study is cohesion and static friction combined in a single parameter. Next, The fractures are compacted during failure, the fault strength recovers, and a new cycle begins (figure 16). Such porosity increase can be compared to the dissolution of calcite in this study, which also causes porosity increase. Other suggested mechanisms of fault weakening were the reduction of friction of asperities by dissolving crystal edges and/or argillilitzation, which roughly corresponds to reducing static friction (Heinicke et al., 2009). The studies of Heinicke et al., (2009) and Vavryčuk & Hrubcová, (2017) show that long term alteration by $CO_2$ saturated water and correlated triggering of seismicity, as occurring is simulations in this study, is realistic. Fault strenght is however found to increase after a rupture event in their studies. In the currently used workflow, healing of cohesion (as also found by van den Ende & Niemeijer, (2019) and static friciton (as also found by (Chen et al., 2015) is not incorporated, but could be implemented if desired.

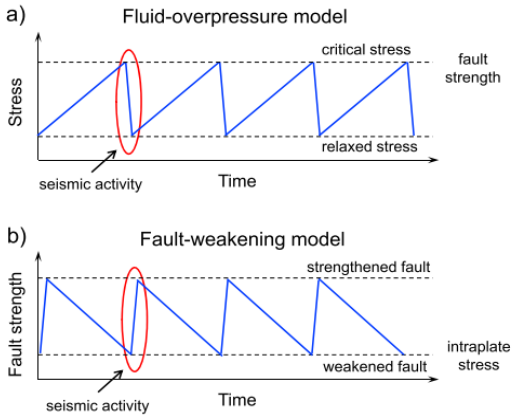


*Figure 16: Illustration of the fault-weakening model of Vavryčuk & Hrubcová (2017). Figure a shows a standard rupture cycle in which stress is built up in a reservoir until criticality is reached and some of the stress is lost. Figure b illustrates how fault weakening could create a similar circular rupture pattern.*

As previously stated, chemical reactions are dependent on site-specific conditions: The pressure, temperature, mineralogy, grain size, spatial distribution of minerals, composition of the brine, water saturation and the starting porosity and permeability (Gaus, 2010). Many studies have focused on unraveling the dissolution and precipitation associated with $CO_2$ injection in brine (e.g. Johnson et al., 2004; Kampman et al., 2014; Lagneau et al., 2005; Xu et al., 2005). Batch reactive modeling studies showed that upon injection of $CO_2$ in glauconitic sandstones Illite and K-feldspar are found to precipitate from dissolving glauconite. Also, carbonate minerals like siderite and ankerite, or to a lesser extent dolomite or dawsonite were found ((Xu et al., 2004). Reactive fluid flow modeling done using geochemical transport code TOUGHREACT found dawsonite and ankerite as the main trapping minerals. Precipitation of siderite and ankerite however requires chlorite and hematite dissolution. Precipitation of dawsonite requires oligoclase dissolution (Xu et al., 2005.). Such precipitation of secondary minerals is thought to influence permeability, porosity and cohesion. Also, the mineralogy of fault gouge largely affects the frictional properties. The extent of these influences is not tested in the workflow of this study, but could significantly influence and improve fault stability, therefore lower influence seismicity accordingly.

Predictions of the extent of such chemical reactions have been made using geochemical modeling codes. Long-term geochemical modeling of Bakker (2017) showed that for a single starting material, dependent on the residence time of the fluid and the refreshment time of the fluid, a vast span of different dynamic friction coefficients and cohesions were found. Their study found for most of the modeling setups that precipitation of dolomite and siderite was expected upon chemical alteration of standard

claystone with initial 25 mass% calcite, a dynamic friction of 0.35 and cohesion of 0.77. Values of $\mu_d$ between 0.27 and 0.51 and cohesion between -1.82 and 4.04 MPa (in which a negative cohesion value was the result of measurement errors) were found in their study. In this study, simulations 3 and 4 are based on 2 possible outcomes from Bakker (2017). Other outcomes in terms of mineralogy, dynamic friction and cohesion could have higher values of $\mu_d$ which would lower the expected moment magnitude of rupture events. Also, cohesion values could be different than the values tested in simulations 6 and 7, changing seismicity accordingly.

Modeling studies (Knauss et al., 2005) and field observations (Kampman et al., 2009) suggest that the dissolution and precipitation processes of different minerals function on different time scales and different spatial locations with respect to the injection well, as shown in figure 17. If any calcite cemented fault were to be located in the near well bore area, leeching of calcite would be possible. In their study, however, $CO_2$-brine is injected rather than pure liquid $CO_2$. In the simulations in this study, the effects shown in figure 17 are expected to operate over a longer range. A lowered pH and reactivity are expected outside of the pure liquid $CO_2$ bubble, where a high concentration of aqueous $CO_2$ is found (previously described as zone 2 and 3). As the $CO_2$ bubble continuously spreads in the simulations, the zone with a low pH and little calcite mass-% (first 100 m in figure 17) is expected to cross the fault in the simulations. Leeching of the fault zone of its calcite is therefore a realistic option if the fault zone has a sufficient porosity and permeability. Care should however be taken in predicting such fluid-mineral reactions as mineral reactions are complex and highly site-specific and the relative flows of $CO_2$ and brine are governed by complex two-phase flow and heterogeneities in geological reservoirs (Kampman et al., 2014).

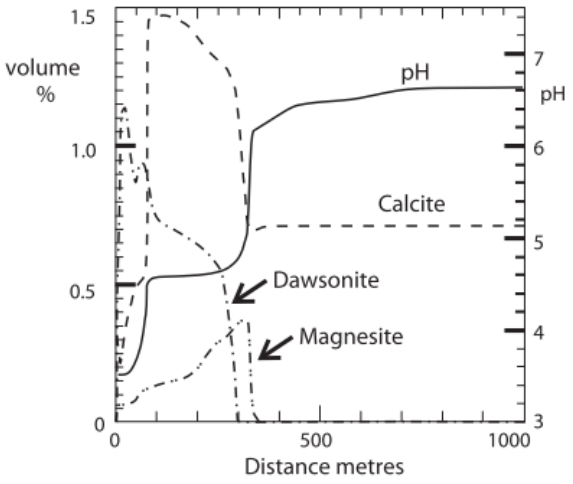


Figure 17: Modelled mineral abundance as a function of *distance along a radial flow path away from an CO2 brine injector in an arkosic sandstone. Close to the injector acid fluids (pH ~3.5) dissolve calcite but further out more evolved fluids have reacted with silicate minerals which increase their pH to ~4.5, leading to calcite precipitation. Figure taken from (Kampman et al., 2014), redrawn from (Knauss et al., 2005)*

The vales taken for injection rate and temperature, which are somewhat unfavourable in this study to create an initial criticality, but do not completely control the extent of chemical reactions. The extent of reactions is largely governed in this study by the assumptions used regarding instantaneous dissolution of calcite equal to the maximum amount of $CO_2$ that has passed a spatiotemporal location, and the assumption that the fault is equally porous and permeable as the reservoir rock. As discussed in the text above, (localized) weakening of fault strength following the dissolution of $CO_2$ is certainly possible under site specific and injection specific conditions. Fault weakening can result in an increase of number or magnitude of rupture events, and the total area that will receive slip during such rupture events. Also, using the assumptions of homogenous fault strength parameters in this study, rupture can continue along the fault into the caprock, potentially affecting storage security.

## Overestimation of reactivity

In this study, important assumptions are taken that calcite dissolves instantaneously, that the maximum $CO_2$ molarity equals the total dissolved calcite, and that the fault zone is equally porous and permeable as the reservoir rock. These assumptions were taken as the actual rates and reactivities are highly site specific (e.g. Kampman et al. (2014)), and too complicated to be predicted using a simple set of equations. The section below discusses the whether these assumptions could be (near) realistic.

Any proposed mechanism above or any other mechanism leading to fault weakening from chemical interaction requires a steady influx of acidity. The presence of acidified water is a main requirement, acting as a host for dissolution and precipitation reactions (Rathnaweera et al., 2015). As the dissolution of minerals in the fault zone buffers the pH, continuous refreshment of the acid is required, which occurs when fault zones or fractures act as a conduit rather than a barrier. Whether a fault zone will act as a conduit, barrier or combined conduit-barrier system is complex, and controlled by the relative percentage of fault core, damage zones structure, variability in grain scale, and fracture permeability (Caine et al., 1996). Roughly speaking, fractures in the damage zone can act as a conduit for fluid transport, whereas fine-grained solidified gouge material usually acts as a barrier. In this study, a fictive fault was modeled without any information regarding the fault's permeability. The fault zone was assumed equally porous and permeable as the surrounding sandstones. Even if the permeability and porosity of the fault zone is relatively high, it is unlikely to match the permeability and porosity of a high-quality reservoir sandstone such as the Ijsselmonde sandstone member. The supply rate of acidity towards the fault zone is most likely overestimated in this study.

However, the supply rate of acidity was not the limiting factor in $CO_2$ reactions in the current setup. Maximum dissolved $CO_2$ concentrations at the fault are found to be ~1.33 mol/kg water (calculated from the TOUGH output), which is slightly below the maximum solubility of ~1.60 mol /kg $CO_2$ in pure water at the in situ P/T conditions of ~30 degrees and ~300 bar at the proximal fault (Duan & Sun, 2003). Assumed is that the maximum concentration of dissolved $CO_2$ that has been present at a certain coordinate point during the simulation equals the amount of $CO_2$ incorporated in reactions at that specific coordinate. Also assumed is that the maximum level of dissolved $CO_2$ corresponds to instantly dissolving calcite according to a 1:1 ratio, which makes the solubility of $CO_2$ the limiting factor in the total amount of reacted calcite in this study. A factor that is neglected in this study but generally shown to influence $CO_2$ dissolution is the salinity of the brine. $CO_2$ storage is done in deep saline aquifers that would be of no further use because of the salinity. The salinity however largely influences the solubility as shown in figure 18. The maximum solubility of $CO_2$ found in current simulations at the proximal fault is ~ 1.33 mol/kg $H_2O$. Maximum solubility at reservoir conditions of ~30° and ~300 bar would correspond to ~1.29, 1.06, or 0.75 mol/kg $H_2O$ for 1 M 2M, and 4M, aqueous NaCl solutions (Duan & Sun, 2003). Increasing salinity of the reservoir in simulations would largely affect total $CO_2$ solubility hence Calcite dissolution. The actual salinity of the lower Cretaceous sandstone reservoirs used as an example reservoir in this study is unknown. Also, the focus of this study is on determining the relative relations between $CO_2$ injection, fault weakening and seismicity rather dan defining the absolute expected seismicity for an actual reservoir. It should nevertheless be noted that when applying actual reservoir conditions regarding salinity, the amount of $CO_2$ that will dissolve will be less, and reaction rates will be slower.

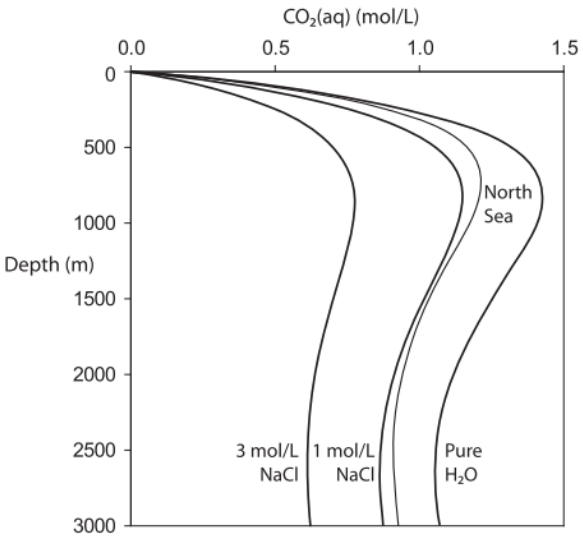


*Figure 18: Figure adapted from Kampman et al. (2014): CO2 solubility as a function of the depth below surface. The solubility profiles are calculated using equations from Duan et al., 2006), using a geothermal gradient of 25 °C/km (slightly lower than the gradient of 28 °C/km used in this study) and hydrostatic pressure gradients. Curves are plotted for fluid salinities of 1 mol/L, 3 mol/ L and a typical North Sea salinity profile of 25,000 ppm/km (Bjørlykke and Gran, 1994)*

## Seismicity

This study has assumed instantaneous slip weakening behaviour. Whether slip occurs seismic or aseismic along calcite faults has been investigated experimentally in the context of $CO_2$ storage (e.g., Rattez et al., (2021); Bakker, (2017)). The study of Rattez et al. (2021) suggest that for wet samples, an

increase in rate and state parameters is expected for degraded samples. While friction coefficients are found to decrease, the seismogenic potential of faults is lowered as the *(a-b)* rate and state parameters tend to increase upon degradation of the calcite. These rate and state parameters basically determines whether unstable velocity weakening slip (*(a-b)*<0) or stable velocity strengthening slip (*(a-b)*>0) will occur upon initiation of slip (Dieterich, 1978, 1979; Ruina, 1983). So, although friction coefficients are lowered, less seismicity is expected. Whether no seismic slip can be expected at all is hard to predict, as other currently operational CCS projects in sandstone aquifers have shown that micro seismicity occurs upon injection (e.g. Couëslan et al. (2014); Trupp et al. (2021); Verdon et al. (2013); White & Foxall, (2016)).

In the Netherlands, seismicity exceeding a magnitude of 1.5-2.0 on the scale of Richter (Local Magnitude) is potentially felt at the surface, potentially damaging houses and undermining public acceptance (Muntendam-Bos et al., 2022). Such local magnitude corresponds to a moment magnitude of ~1.6 – 2.0 following a conversion formula based on seismicity measurements from the Groningen gas field (Dost et al., 2016). In other words, seismicity below Mw ~1.6 is usually not felt but can still be undesired. In all simulations, including the base case without $CO_2$ influence, rupture events were noted as Mw > 2.5. The absolute values of injection rate or temperature as used in this study should therefore not be used for actual $CO_2$ injection.

In this study, an injection rate of 4 Mt/y was adapted to create a stress level leading to criticality at the fault, which is unusually high if only one injection well were to be used. However, for the development of a pressure front at the porosity and permeability used in the simulations in this study, it hardly matters whether 1 injection well is used or whether the same amount is spread over a few close wells. According to Neele et al. (2013), an average injection rate in the P/Q field lower Cretaceous sandstones of 10 Mt/y is estimated to be possible. The seismicity and uniform pressure increase resulting from the injection of 4 Mt/y this study shows that an injection rate of 10 Mt/y would have to be spread over multiple injection wells which are located far (tens of kilometres, according to Neele et al. (2013)) from other injection locations prevent extreme pressure increases and thus seismic risk. Also, seismic surveying will have to tell whether any major visible faults are located within the well area. This is a key point, as not all faults are easily found in seismic surveys, but knowledge about any close faults to the injection well can be crucial.

In this study, seismicity was found of moment magnitude between -3 and 3.19. The rupture events between 1.57 and 3.19 found in this study are problematic and could do significant damage to infrastructure or public acceptance of CCS. In the largest recorded rupture event (3.19 Mw, simulation 2 of the fault at 600 m, figure 14) it is visible that over 84.1% of the fault area experienced slip, and it seems that the ruptured area and thus magnitude of the event could have been higher if the modelled fault surface area would have been larger in the direction of the y-axis. Such main events in the simulation require significant area and distance of slip along the fault surface. The moment magnitude is a function of slip area and average slip distance, whereas slip distance is a function of the stress drop on a single patch For simulations with a higher stress drop (e.g., simulations 3, 4, and 7) slip distance will determine mostly the magnitude of the rupture. For simulations with a lowered stress drop (simulations 2,5 and 6) slip area will determine the magnitude of the rupture. As shown in results, the minimum fault surface required to create a stress drop of 1.35 Mw corresponds to a 125 m by 125 m surface. The minimum fault size required for triggering seismicity felt at the surface is therefore quite significant. The average resolution of seismic imaging is $1/4^{th}$ of the wavelength $\lambda$ of the signal, (Schulte et al., 2019), corresponding to 25 to 50 m, depending on the depth and material properties. So, depending on the orientation of the fault, most 125 x 125 m faults should be visible in a standard seismic interpretation study. Difficulty in interpretation arises when the orientation of the fault is near vertical, when normal faults have become inverted, or when e.g., the weak zones in the rock consist of tensile cracks filled with calcite cement. According to Zoback (2007) the crust can be considered as containing many faults and weaknesses at various orientations, of which only some are optimally oriented for

frictional sliding. Also, as issued by Faulkner et al. (2006) rupture along such random oriented weaker faults in zones can be triggered below critical stress due to stress rotation and long range elastic stresses from other slipping faults. In current seismic risk assessments, the risk of missing randomly oriented yet near critically stressed faults in such seismic interpretation is accounted for. In this study, it is shown that also the risk of chemically weakening such unidentified faults should be taken in account.

## Continuation and application of this study

The currently used combination of individual models that contribute to the workflow is found to be useful for the first determination of the relative influence of temperature, pressure, and $CO_2$ reactivity on fault reactivation. On top of that individual chemical influences on seismicity could be tested using relatively simple linear relations between $CO_2$ concentration and static/dynamic friction weakening /strengthening and cohesion. Both uses of the current setup however could be significantly improved in model complexity. On the flow and $CO_2$ concentration side of the research, improvements can be made by implementing reactive flow modelling in the setup. A good example of such model is TOUGHREACT a reactive geochemical transport code (Xu and Pruess, 1998, 2001), which is shown to work for $CO_2$ sequestration in sandstone/shale reservoirs by Xu et al. (2005). Minor adaptions to the scripts and workflow used in this study would be required to implement TOUGHREACT as it describes both 2 phase flow as chemical reactions. Other kinds of reactive modelling numerical codes are GEM or PHREEQC. Of these three numerical codes, GEM and PHREEQC were found to be in best agreement when compared to experimental brine-$CO_2$-water reactions (Gundogan et al., 2011). Enhanced knowledge on the dissolution and precipitation of minerals in the simulations should on its turn be coupled to a more in-depth study of fault mineralogical composition and fault strength.

An interesting continuation of this study would be the implementation of seismicity equations honoring Dieterich-type of slip behaviour (Dieterich, 1978, 1979; Ruina, 1983). In the current model setup, instantaneous slip weakening behaviour is assumed and any slip is assumed to result in seismicity. It would be interesting to see whether implementing rate and state parameters and time dependent slip weakening or strengthening would result in similar seismicity.

In the current setup of the study, a lot of assumptions and parameters are used which all individually could influence the outcome of the study. It would be of great interest to perform probabilistic modelling within the ranges of such currently fixed parameters. Important questions are how the currently chosen injection parameters like injection rate, temperature, composition but also reservoir properties like bottomhole pressure, salinity, pressure and stress gradients, porosity, permeability, etc. influence the outcome of this study.

Another suggestion for further research is regarding the current knowledge of the lower Cretaceous sandstone reservoirs used in this study. Although the area is featured in multiple screenings regarding options for offshore $CO_2$ storage, relatively little is known about the exact properties of the reservoir of the sandstone. Many assumptions were taken in this study regarding the mineralogy, porosity, permeability, rock/ gouge strength, and heterogeneity of these parameters. Before further development of the reservoir, it would be advised to perform test drills in the area to gain better constrain on such parameters. New, more accurate data should then be used to re-evaluate the geomechanical stability of the reservoir and faults. Another suggestion is the coupling of the modelling workflow to the possibilities above ground. It would be useful to couple the used injection pressure/ temperature to a model describing what infrastructure would be needed to reach such injection conditions. Using current technology, are injection rates of up to 4 Mt/y possible at the required pressure to push the $CO_2$ into the reservoir? And if possible, are the conditions used in this study desirable in terms of costs of the operations? The questions regarding injection infrastructure, but also those regarding site characterization are part of a standard sequence of steps that must be followed prior to development of CCS projects in virgin saline aquifers (Neele et al., 2013). In other words, the workflow used in this

study could serve as an addition to the geomechanically and seismic risk evaluation that is part of a site characterization study in the development plan of a CCS project in saline aquifers.

In current seismic risk assessments prior to CCS projects, geochemical modeling is often mentioned and sometimes performed. For example in the seismic risk assessment of the Dutch P-18 gas field $CO_2$ storage project (CATO-2), geochemical modeling only focused on porosity/permeability changes influencing infectivity, and long term solubility trapping/ mineral trapping mechanisms, but did not focus on potential weakening of pre-existing faults (Neele et al., 2020). In the Storage Risk Assessment (SRA) of the K-4 field in the United Kingdom (White Rose, 2016), only 'lubrication' of pre-existing faults by migration of $CO_2$ is mentioned, yet found unlikely as the maximum expected $CO_2$ pressure is below the measured fracture closure pressure. Geochemical modelling is mainly performed in the SRA of the K-4 field to assess whether geochemical reactions could influence the maximum storage capacity through compartmentalization of the reservoir or whether geochemical reactions could influence bulk rock strength (not fault strength). Experiments to test geochemical effects on rock strength were performed in the SRA of the Peterhead CCS project, even as geochemical batch modelling (Shell, 2015). Their study did perform a coupled reactive transport study which suggested no significant changes in mineralogy in the long-term following their mineralogy. However, the possibility of pre-existing weaker zones in the form of fault was not explored in their study. This study has shown that significant changes in frequency, timing and magnitude of seismicity can be expected if either frictional parameters or cohesion values are chemically altered. The potential of $CO_2$ to locally weaken fault under circumstances of conducting faults, high pressures, low temperatures and certain mineralogies should be taken in account in future seismic risk assessments.

# Conclusions

The workflow described is useful for quick analysis of simplified reservoirs and faults regarding the spatiotemporal relations between temperature, pressure, and $CO_2$ saturation. Absolute values of chemical weakening of $\mu_s$, $\mu_d$ or $S_o$, or absolute values of rupture magnitude, frequency or timing from this study cannot be used. Relative relationships linking the development of stresses and $CO_2$ saturation, corresponding chemical weakening of faults and seismicity resulting from that can be tested successfully in the current study setup.

Pressure increases lead to a uniform decrease of effective stresses following the pore pressure and increase poro-elastic stresses. These effects are influencing a large area within reservoirs. Thermo-elastic effects following a temperature drop are found on a more local scale, largely influencing the shear strength. Both largely affect fault strength and can potentially trigger seismicity. Chemical weakening resultant from $CO_2$ can only act as a triggering mechanism of seismicity when $\mu_s$ or $S_o$ values are lowered.

Lowering static friction lowers the influence of effective normal stress on rock strength and lowers the required stresses to reach criticality. A lowered stress drop occurs upon rupture, and thus slip distance at certain patches along a fault surface is lowered. Lowering static friction has an enhancing effect on the area that will slip upon rupture.

Chemically altering dynamic friction is found to only change the seismicity once initial rupture events have been noted. Lowering the dynamic friction of fault gouge will increase the stress drop upon rupture along a single patch of the fault. Such increased stress drop along a single patch will affect the rest of the fault surface and potentially trigger continuation of the rupture along the fault. Lowering dynamic friction causes rupture events of higher magnitude and lower frequency.

Lowering cohesion values will reduce the time required to build up stress to reach a critical state. $CO_2$ interactions can create an area of chemically weakened rock, which is more prone to slip. No further effects are noted as cohesion is lost upon rupture.

Static friction, dynamic friction, and cohesion all show a different relationship towards the number, frequency, and timing of rupture events once chemically altered. Therefore the 3 should be investigated separately when investigating the rupture potential of faults in the context of $CO_2$ storage. Which chemical effect has most effect on the seismicity largely depends on the parameters used in the study, but lowering dynamic friction is clearly found to increase the rupture magnitude most.

If only a localized part of the fault chemically weakens, and slip is triggered locally, long-range elastic stress redistribution can cause the continuation of slip on other parts of the fault. Such continuation of slip increases the rupture area and thus 1) increases rupture magnitude 2) can compromise sealing capacity if rupture is found to continue in the caprock. The potential of $CO_2$ to locally weaken a fault's $\mu_s$, $\mu_d$ or $S_o$ under certain circumstances should be taken in account in future seismic risk assessments.

## Acknowledgements

This study has been bade possible by TNO Utrecht, team Geomechanics, AGS, TNO-GDN. Supervisors of the thesis Sander Osinga and André Niemeijer are thanked for their supervision and constructive discussions. Thibault Candela is thanked for his assistance in preparing BSQuakeSim and many constructive discussions. Also Peter Fokker is thanked for his assistance in setting up SRIMA. Daniel Loeve is thanked for assistance in setting up TOUGH.

# References

Bakker, E. (2017). Frictional and transport properties of simulated faults in CO2 storage reservoirs and clay-rich caprocks (Doctoral dissertation, UU Dept. of Earth Sciences), 178-223

Bakker, E., Hangx, S. J. T., Niemeijer, A. R., & Spiers, C. J. (2016). Frictional behaviour and transport properties of simulated fault gouges derived from a natural CO2 reservoir. International Journal of Greenhouse Gas Control, 54, 70–83. https://doi.org/10.1016/j.ijggc.2016.08.029

Bakx, E., Buijze, L., Wassing, B., (2022). Formation, lithology and region-specific stress field in the Netherlands. Implications for fault stability in geothermal doublets. Pers. comm.

Bedford, J. D., Faulkner, D. R., & Lapusta, N. (2022). Fault rock heterogeneity can produce fault weakness and reduce fault stability. Nature Communications, 13(1), 1–7. https://doi.org/10.1038/s41467-022-27998-2

Bickle, M., Kampman, N., & Wigley, M. (2013). Natural analogues. Reviews in Mineralogy and Geochemistry, 77(1), 15–71. https://doi.org/10.2138/rmg.2013.77.2

Bjørlykke, K., & Gran, K. (1994). Salinity variations in North Sea formation waters: Implications for large-scale fluid movements. Marine and Petroleum Geology, 11(1), 5-9.

Buijze, L., Fokker, P. A., & Wassing, B. (2021). Quantification of induced seismicity potential of geothermal operations Analytical and numerical model approaches FINAL REPORT by. december.

Caine, J. S., Evans, J. P., & Forster, C. B. (1996). Fault zone architecture and permeability structure. Geology, 24(11), 1025–1028. https://doi.org/10.1130/0091-7613(1996)024<1025:FZAAPS>2.3.CO;2

Canal, J., Delgado-Martín, J., Barrientos, V., Juncosa, R., Rodríguez-Cedrún, B., & Falcón-Suarez, I. (2014). Effect of supercritical CO2 on the Corvio sandstone in a flow-thru triaxial experiment. Rock Engineering and Rock Mechanics: Structures in and on Rock Masses - Proceedings of EUROCK 2014, ISRM European Regional Symposium, May, 1357–1362. https://doi.org/10.1201/b16955-236

Candela, T., Peters, E., Van Wees, J. D., Fokker, P., & Wassing, B. (2019). Effect of fault roughness on injection-induced seismicity.

Candela, T., Peters, E., Van Wees, J. D., Fokker, P., Wassing, B., & Ampuero, J. P. (2019). Effect of fault roughness on injection-induced seismicity. In 53rd US Rock Mechanics/Geomechanics Symposium. OnePetro.

Chang, C., Zoback, M. D., & Khaksar, A. (2006). Empirical relations between rock strength and physical properties in sedimentary rocks. Journal of Petroleum Science and Engineering, 51(3–4), 223–237. https://doi.org/10.1016/j.petrol.2006.01.003

Chen, J., Verberne, B. A., & Spiers, C. J. (2015). Interseismic re-strengthening and stabilization of carbonate faults by "non-Dieterich" healing under hydrothermal conditions. Earth and Planetary Science Letters, 423, 1–12. https://doi.org/10.1016/j.epsl.2015.03.044

Couëslan, M. L., Butsch, R., Will, R., & Locke, R. A. (2014). Integrated reservoir monitoring at the Illinois Basin - Decatur Project. Energy Procedia, 63, 2836–2847. https://doi.org/10.1016/j.egypro.2014.11.306

Dieterich, J. H. (1978). Time-dependent friction and the mechanics of stick-slip. In Rock friction and earthquake prediction (pp. 790-806). Birkhäuser, Basel.

Dieterich, J. H. (1979). Modeling of rock friction: 1. Experimental results and constitutive equations. Journal of Geophysical Research: Solid Earth, 84(B5), 2161-2168.

Dost, B., Edwards, B., & Bommer, J. J. (2016). Local and Moment Magnitudes in the Groningen Field. June.

Duan, Z., & Sun, R. (2003). An improved model calculating CO 2 solubility in pure water and aqueous NaCl solutions from 273 to 533 K and from 0 to 2000 bar. Chemical Geology 193.3-4, 257–271. www.elsevier.com/locate/chemgeo

Duan, Z., Sun, R., Zhu, C., & Chou, I. M. (2006). An improved model for the calculation of CO2 solubility in aqueous solutions containing Na+, K+, Ca2+, Mg2+, Cl−, and SO42−. Marine chemistry, 98(2-4), 131-139.

Erickson, K. P., Lempp, C., & Pöllmann, H. (2015). Geochemical and geomechanical effects of scCO2 and associated impurities on physical and petrophysical properties of Permotriassic Sandstones (Germany): an experimental approach. Environmental Earth Sciences, 74(6), 4719–4743. https://doi.org/10.1007/s12665-015-4437-0

Faulkner, D. R., Mitchell, T. M., Healy, D., & Heap, M. J. (2006). Slip on "weak" faults by the rotation of regional stress in the fracture damage zone. Nature, 444(7121), 922–925. https://doi.org/10.1038/nature05353

Gaus, I. (2010). Role and impact of CO2-rock interactions during CO2 storage in sedimentary rocks. In International Journal of Greenhouse Gas Control (Vol. 4, Issue 1, pp. 73–89). https://doi.org/10.1016/j.ijggc.2009.09.015

Geel, K., Verdel, A., Paap, B., & Orlic, B. (2021). Feasibility of large-scale CO2 storage in aquifers: performance of DAS technology and pressure limits for safe injection.

Gundogan, O., Mackay, E., & Todd, A. (2011). Comparison of numerical codes for geochemical modelling of CO2 storage in target sandstone reservoirs. Chemical Engineering Research and Design, 89(9), 1805–1816. https://doi.org/10.1016/j.cherd.2010.09.008

Hangx, S., Bakker, E., Bertier, P., Nover, G., & Busch, A. (2015). Chemical-mechanical coupling observed for depleted oil reservoirs subjected to long-term CO2-exposure - A case study of the Werkendam natural CO2 analogue field. Earth and Planetary Science Letters, 428, 230–242. https://doi.org/10.1016/j.epsl.2015.07.044

Hangx, S. J. T., & Spiers, C. J. (2009). Reaction of plagioclase feldspars with CO2 under hydrothermal conditions. Chemical Geology, 265(1–2), 88–98.

https://doi.org/10.1016/j.chemgeo.2008.12.005

Hangx, S., Spiers, C., & Peach, C. (2009). The mechanical behavior of anhydrite and the effect of CO2 injection. Energy Procedia, 1(1), 3485–3492. https://doi.org/10.1016/j.egypro.2009.02.140

Hangx, S., van der Linden, A., Marcelis, F., & Bauer, A. (2013). The effect of CO2 on the mechanical properties of the Captain Sandstone: Geological storage of CO2 at the Goldeneye field (UK). International Journal of Greenhouse Gas Control, 19, 609–619. https://doi.org/10.1016/j.ijggc.2012.12.016

Harper, M. L. (1971). Approximate geothermal gradients in the North Sea basin. Nature, 230(5291), 235–236. https://doi.org/10.1038/230235a0

Heinicke, J., Fischer, T., Gaupp, R., Götze, J., Koch, U., Konietzky, H., & Stanek, K. P. (2009). Hydrothermal alteration as a trigger mechanism for earthquake swarms: The Vogtland/NW Bohemia region as a case study. Geophysical Journal International, 178(1), 1–13. https://doi.org/10.1111/j.1365-246X.2009.04138.x

Hunfeld, L. B., Chen, J., Hol, S., Niemeijer, A. R., & Spiers, C. J. (2020). Healing Behavior of Simulated Fault Gouges From the Groningen Gas Field and Implications for Induced Fault Reactivation. Journal of Geophysical Research: Solid Earth, 125(7). https://doi.org/10.1029/2019JB018790

IEA. (2021). Global Energy Review 2019. Global Energy Review 2019. https://doi.org/10.1787/90c8c125-en

Johnson, J. W., Nitao, J. J., & Knauss, K. G. (2004). Reactive transport modelling of CO 2 storage in saline aquifers to elucidate fundamental processes, trapping mechanisms and sequestration partitioning. Geological Society Special Publication, 233, 107–128. https://doi.org/10.1144/GSL.SP.2004.233.01.08

Kampman, N., Bickle, M. J., Maskell, A., Chapman, H. J., Evans, J. P., Purser, G., Zhou, Z., Schaller, M. F., Gattacceca, J. C., Bertier, P., Chen, F., Turchyn, A. V., Assayag, N., Rochelle, C., Ballentine, C. J., & Busch, A. (2014). Drilling and sampling a natural CO2 reservoir: Implications for fluid flow and CO2-fluid-rock reactions during CO2 migration through the overburden. Chemical Geology, 369, 51–82. https://doi.org/10.1016/j.chemgeo.2013.11.015

Kampman, N., Bickle, M., Becker, J., Assayag, N., & Chapman, H. (2009). Feldspar dissolution kinetics and Gibbs free energy dependence in a CO2-enriched groundwater system, Green River, Utah. Earth and Planetary Science Letters, 284(3–4), 473–488. https://doi.org/10.1016/j.epsl.2009.05.013

Kampman, N., Bickle, M., Wigley, M., & Dubacq, B. (2014). Fluid flow and CO2-fluid-mineral interactions during CO2-storage in sedimentary basins. In Chemical Geology (Vol. 369, pp. 22–50). https://doi.org/10.1016/j.chemgeo.2013.11.012

Kim, K., Vilarrasa, V., & Makhnenko, R. Y. (2018). CO 2 injection effect on geomechanical and flow properties of calcite-rich reservoirs. Fluids, 3(3). https://doi.org/10.3390/fluids3030066

Knauss, K. G., Johnson, J. W., & Steefel, C. I. (2005). Evaluation of the impact of CO2, co-contaminant gas, aqueous fluid and reservoir rock interactions on the geologic sequestration of CO2. Chemical Geology, 217(3-4 SPEC. ISS.), 339–350. https://doi.org/10.1016/j.chemgeo.2004.12.017

Lagneau, V., Pipart, A., & Catalette, H. (2005). Reactive Transport Modelling of CO2 Sequestration in Deep Saline Aquifers. In Oil & Gas Science and Technology-Rev. IFP (Vol. 60, Issue 2).

Lamy-Chappuis, B., Angus, D., Fisher, Q., Grattoni, C., & Yardley, B. W. D. (2013). enriched brine injection. Figure 1, 399–406. https://doi.org/10.1002/2013GL058534.Received

Lamy-Chappuis, B., Angus, D., Fisher, Q. J., & Yardley, B. W. D. (2016). The effect of CO2-enriched brine injection on the mechanical properties of calcite-bearing sandstone. International Journal of Greenhouse Gas Control, 52, 84–95. https://doi.org/10.1016/j.ijggc.2016.06.018

Marbler, H., Erickson, K. P., Schmidt, M., Lempp, C., & Pöllmann, H. (2013). Geomechanical and geochemical effects on sandstones caused by the reaction with supercritical CO2: An experimental approach to in situ conditions in deep geological reservoirs. Environmental Earth Sciences, 69(6), 1981–1998. https://doi.org/10.1007/s12665-012-2033-0

Metz, B., Davidson, O., De Coninck, H. C., Loos, M., & Meyer, L. (2005). IPCC special report on carbon dioxide capture and storage. Cambridge: Cambridge University Press.

Muntendam-Bos, A. G., Hoedeman, G., Polychronopoulou, K., Draganov, D., Weemstra, C., van der Zee, W., Bakker, R. R., & Roest, H. (2022). An overview of induced seismicity in the Netherlands. Netherlands Journal of Geosciences, 101, e1. https://doi.org/10.1017/njg.2021.14

National Climate Agreement. (2019) from: https://www.klimaatakkoord.nl/documenten/publicaties/2019/06/28/national-climate-agreement-the-netherlands

Neele, F., ten Veen, J., Wilschut, F., & Hofstee, C. (2012). Independent assessment of high-capacity offshore CO2 storage options. TNO Report, TNO-060-UT, 93. http://cdn.globalccsinstitute.com/sites/default/files/publications/35621/independent-assessment-high-capacity-offshore-co2-storage-options-opt.pdf

Neele, F., Hofstee, C., Arts, R., Vandeweijer, V., Nepveu, M., Veen, J. Ten, & Wilschut, F. (2013). Offshore storage options for CO2 in the Netherlands. Energy Procedia, 37, 5220–5229. https://doi.org/10.1016/j.egypro.2013.06.438

Neele, F., Wildenborg, T., Geel, K., Loeve, D., Peters, L., Kahrobaei, S., Candela, T., Koenen, M., Hopmans, P., Van Der Valk, K., Orlic, B., & Vandeweijer, V. (2020). CO2 storage feasibility in the P18-6 depleted gas field. www.tno.nl

Nikkhoo, M., & Walter, T. R. (2015). Triangular dislocation: an analytical, artefact-free solution. Geophysical Journal International, 201(2), 1119-1141.

NOAA. (2021). Despite pandemic shutdowns, carbon dioxide and methane surged in 2020 - Welcome to NOAA Research. Research.noaa.gov. Retrieved 19 July 2022, from https://research.noaa.gov/article/ArtMID/587/ArticleID/2742/Despite-pandemic-shutdowns-carbon-dioxide-and-methane-surged-in-2020.

Nouailletas, O., Perlot, C., La Borderie, C., Rousseau, B., & Ballivy, G. (2013). Shear Behavior Evolution of a Fault due to Chemical Degradation of Roughness: Application to the Geological Storage of CO2. Geomechanics in CO, 2013, 95–114. https://doi.org/10.1002/9781118577424.ch6

Nover, G., Von Der Gönna, J., Heikamp, S., & Köster, J. (2013). Changes of petrophysical properties of sandstones due to interaction with supercritical carbon dioxide – a laboratory study. European Journal of Mineralogy, 25(3), 317–329. https://doi.org/10.1127/0935-1221/2013/0025-2295

Pluymakers, A. M. H., Samuelson, J. E., Niemeijer, A. R., & Spiers, C. J. (2014). Effects of temperature and CO2 on the frictional behavior of simulated anhydrite fault rock. Journal of Geophysical Research: Solid Earth, 119(12), 8728–8747. https://doi.org/10.1002/2014JB011575

Pruess, K. (2011). ECO2M: a TOUGH2 fluid property module for mixtures of water, NaCl, and CO2, including super-and sub-critical conditions, and phase change between liquid and gaseous CO2 (No. LBNL-4590E). Lawrence Berkeley National Lab.(LBNL), Berkeley, CA (United States).

Pruess, K., Oldenburg, C., & Moridis, G. (1999). TOUGH2 User's Guide. Report LBNL-43134,

September, 210.

Pruess, K., Oldenburg, C., & Moridis, G. (2012). TOUGH2 User's Guide, Version 2.0, Report LBNL-43134, Lawrence Berkeley National Laboratory, Berkeley, Calif. Superseded by Pruess et al, 1999.

Rathnaweera, T. D., Ranjith, P. G., Perera, M. S. A., Haque, A., Lashin, A., Al Arifi, N., Chandrasekharam, D., Yang, S. Q., Xu, T., Wang, S. H., & Yasar, E. (2015). CO2-induced mechanical behaviour of Hawkesbury sandstone in the Gosford basin: An experimental study. Materials Science and Engineering A, 641, 123–137. https://doi.org/10.1016/j.msea.2015.05.029

Purcaru, G., & Berckhemer, H. (1978). A magnitude scale for very large earthquakes. Tectonophysics, 49(3-4), 189-198.198.

Rattez, H., Disidoro, F., Sulem, J., & Veveakis, M. (2021). Influence of dissolution on long-term frictional properties of carbonate fault gouge. Geomechanics for Energy and the Environment, 26. https://doi.org/10.1016/j.gete.2021.100234

Rimmelé, G., Barlet-Gouédard, V., & Renard, F. (2010). Evolution of the petrophysical and mineralogical properties of two reservoir rocks under thermodynamic conditions relevant for CO2 geological storage at 3 km depth. Oil and Gas Science and Technology, 65(4), 565–580. https://doi.org/10.2516/ogst/2009071

RIVM. (2021). Daling uitstoot CO2 en luchtverontreiniging zet door in 2020, uitstoot ammoniak stijgt licht. https://www.rivm.nl. Retrieved 9 August 2022, from https://www.rivm.nl/nieuws/daling-uitstoot-co2-en-luchtverontreiniging-zet-door-in-2020-uitstoot-ammoniak-stijgt-licht.

Rohmer, J., Pluymakers, A., & Renard, F. (2016). Mechano-chemical interactions in sedimentary rocks in the context of CO2 storage: Weak acid, weak effects? In Earth-Science Reviews (Vol. 157, pp. 86–110). Elsevier B.V. https://doi.org/10.1016/j.earscirev.2016.03.009

Ruina, A. (1983). Slip instability and state variable friction laws. Journal of Geophysical Research, 88(B12), 10359–10370. https://doi.org/10.1029/JB088iB12p10359

Rutqvist, J., Cappa, F., Rinaldi, A. P., & Godano, M. (2014). Modeling of induced seismicity and ground vibrations associated with geologic CO2 storage, and assessing their effects on surface structures and human perception. International Journal of Greenhouse Gas Control, 24, 64–77. https://doi.org/10.1016/j.ijggc.2014.02.017

Samuelson, J., & Spiers, C. J. (2012). Fault friction and slip stability not affected by Co2 storage: Evidence from short-term laboratory experiments on North Sea reservoir sandstones and caprocks. International Journal of Greenhouse Gas Control, 11(SUPPL), 78–90. https://doi.org/10.1016/j.ijggc.2012.09.018

Schulte, B. W. M., Lyatsky, H., & Bridge, D. (2019). Methods of fault detection with geophysical data and surface geology. Canadian Journal of Exploration Geophysics, 44(5), 1–23. https://csegrecorder.com/articles/view/methods-of-fault-detection-with-geophysical-data-and-surface-geology

Shell. (2015). Peterhead CCS Project. 1–73.

SodM, (2018), from: https://www.sodm.nl/documenten/wob-verzoek/2018/09/21/besluit-wob-verzoek-inzake-waterinjectieput-van-vermilion-locatie-nijensleek-westerveld

Tenthorey, E., & Cox, S. F. (2006). Cohesive strengthening of fault zones during the interseismic period: An experimental study. Journal of Geophysical Research: Solid Earth, 111(9). https://doi.org/10.1029/2005JB004122

TNO-GDN (2022). IJsselmonde Sandstone Member. In: Stratigraphic Nomenclature of the Netherlands, TNO – Geological Survey of the Netherlands. Accessed on 29-07-2022 from

http://www.dinoloket.nl/en/stratigraphic-nomenclature/ijsselmonde-sandstone-member.

Trupp, M., Ryan, S., Barranco, I., Leon, D., & Scoby-Smith, L. (2021). Developing the world's largest CO 2 Injection System-a history of the Gorgon Carbon Dioxide Injection System. https://ssrn.com/abstract=3815492

van den Ende, M. P. A., & Niemeijer, A. R. (2019). An investigation into the role of time-dependent cohesion in interseismic fault restrengthening. Scientific Reports, 9(1). https://doi.org/10.1038/s41598-019-46241-5

van der Meer, L. G. H., & Yavuz, F. (2009). CO2 storage capacity calculations for the Dutch subsurface. Energy Procedia, 1(1), 2615–2622. https://doi.org/10.1016/j.egypro.2009.02.028

Vavryčuk, V., & Hrubcová, P. (2017). Seismological evidence of fault weakening due to erosion by fluids from observations of intraplate earthquake swarms. Journal of Geophysical Research: Solid Earth, 122(5), 3701–3718. https://doi.org/10.1002/2017JB013958

Verdon, J. P., Kendall, J. M., Stork, A. L., Chadwick, R. A., White, D. J., & Bissell, R. C. (2013). Comparison of geomechanical deformation induced by megatonne-scale CO2 storage at Sleipner, Weyburn, and In Salah. Proceedings of the National Academy of Sciences of the United States of America, 110(30). https://doi.org/10.1073/pnas.1302156110

Vilarrasa, V. (2016). The role of the stress regime on microseismicity induced by overpressure and cooling in geologic carbon storage. Geofluids, 16(5), 941–953. https://doi.org/10.1111/gfl.12197

Vilarrasa, Víctor, Carrera, J., Olivella, S., Rutqvist, J., & Laloui, L. (2019). Induced seismicity in geologic carbon storage. Solid Earth, 10(3), 871–892. https://doi.org/10.5194/se-10-871-2019

Vilarrasa, Víctor, Silva, O., Carrera, J., & Olivella, S. (2013). Liquid CO2 injection for geological storage in deep saline aquifers. International Journal of Greenhouse Gas Control, 14, 84–96. https://doi.org/10.1016/j.ijggc.2013.01.015

White, J. A., & Foxall, W. (2016). Assessing induced seismicity risk at CO2 storage projects: Recent progress and remaining challenges. International Journal of Greenhouse Gas Control, 49, 413–424. https://doi.org/10.1016/j.ijggc.2016.03.021

White Rose. (2016). February 2016 K42 : Storage Risk Assessment , Monitoring and Corrective Measures Reports Category : Storage. February.

Xu, T., Apps, J. A., & Pruess, K. (2004). Numerical simulation of CO2 disposal by mineral trapping in deep aquifers. Applied Geochemistry, 19(6), 917–936. https://doi.org/10.1016/j.apgeochem.2003.11.003

Xu, T., Apps, J. A., & Pruess, K. (2005). Mineral sequestration of carbon dioxide in a sandstone-shale system. Chemical Geology, 217(3-4 SPEC. ISS.), 295–318. https://doi.org/10.1016/j.chemgeo.2004.12.015

Xu, T., Pruess, K., (1998). Coupled modeling of non-isothermal multiphase flow, solute transport and reactive chemistry in porous and fractured media: 1. Model development and validation. Lawrence Berkeley National Laboratory Report LBNL-42050, Berkeley, California, 38 pp.

Xu, T., Pruess, K., (2001). Modeling multiphase non-isothermal fluid flow and reactive geochemical transport in variably saturated fractured rocks: 1. Methodology. Am. J. Sci. 301, 16–33.

Zhang, L., Wang, Y., Miao, X., Gan, M., & Li, X. (2019). Geochemistry in geologic CO2 utilization and storage: A brief review. In Advances in Geo-Energy Research (Vol. 3, Issue 3, pp. 304–313). Yandy Scientific Press. https://doi.org/10.26804/ager.2019.03.08

Zhang, W., Li, Y., Xu, T., Cheng, H., Zheng, Y., & Xiong, P. (2009). Long-term variations of CO2 trapped in different mechanisms in deep saline formations: A case study of the Songliao Basin,

China. International Journal of Greenhouse Gas Control, 3(2), 161–180. https://doi.org/10.1016/j.ijggc.2008.07.007

Zoback, M. D. (2007). Rock failure in compression, tension and shear. Reservoir Geomechanics, 127-131

# Appendix

Text in file for TOUGH2-ECO2M module used in this study.

```
2d radial flow realize
ROCKS----1----*----2----*----3----*----4----*----5----*----6----*----7----*----8
Capro    3    2650.0     0.005   9.9E-19   9.9E-19   9.9E-24       2.0    1000.0
     5.e-9       0.0       2.0       0.0       0.0
   13            0.99      0.10      0.01       3.
    8            0.347     0.2985    3.0E-5    1.0E9       1.0
Reale    3    2500.0     0.25   9.87E-13  9.87E-13  9.87E-13       2.0    1000.0
     5.e-9       0.0       2.0       0.0       0.0
   13            0.3       0.10      0.01       3.
    8            0.347     0.2985    3.0E-5    1.0E9       1.0
Realw    3    1.0E50     0.25   9.87E-13  9.87E-13  9.87E-13       2.0    1000.0
     5.e-9       0.0       2.0       0.0       0.0
   13            0.3       0.10      0.01       3.
    8            0.347     0.2985    3.0E-5    1.0E9       1.0
Basro    3    2100.0     0.005   9.9E-19   9.9E-19   9.9E-24       2.0    1000.0
     5.e-9       0.0       2.0       0.0       0.0
   13            0.99      0.10      0.01       3.
    8            0.347     0.2985    3.0E-5    1.0E9       1.0

MULTI----1----*----2----*----3----*----4----*----5----*----6----*----7----*----8
    3    4    4    6
SELEC....2....3....4....5....6....7....8....9...10...11...12...13...14...15...16
    1                                   4    0    0    0    0    0    0    0
        .8        .8     1.e-3     1.e-3
SOLVR----1----*----2----*----3----*----4----*----5----*----6----*----7----*----8
5  Z2   O3    5.0e-2    1.0e-8
START----1----*----2----*----3----*----4----*----5----*----6----*----7----*----8
----*----1 MOP: 123456789*123456789*1234 ---*----5----*----6----*----7----*----8
INDEX
PARAM----1----*----2----*----3----*----4----*----5----*----6----*----7----*----8
   19999     1001000301000000 14    2
         1    1.60E9       -1.                          9.81       6.0
       1.
     1.E-4     1.E00
    5
            2.3602e7                  .01                0.20                40.
INDOM----1----*----2----*----3----*----4----*----5----*----6----*----7----*----8
Capro    1
            2.3602e7              .01e-4              .01e-4                77.0
Reale    1
            2.3613e7              .01e-4              .01e-4                78.8
Realw    1
            2.3613e7              .01e-4              .01e-4                78.8
Basro    1
            2.4594e7              .01e-4              .01e-4                80.8

INCON----1----*----2----*----3----*----4----*----5----*----6----*----7----*----8
F 1 1    1                    1
            2.3613e7              .01e-4              .01e-5                78.8
G 1 1    1                    1
            2.3652e7              .01e-4              .01e-5                78.8
H 1 1    1                    1
            2.3750e7              .01e-4              .01e-5                78.8
I 1 1    1                    1
            2.3848e7              .01e-4              .01e-5                78.8
```

```
J 1 1    1                    1
                2.3946e7              .01e-4              .01e-5                  78.8
K 1 1    1                    1
                2.4044e7              .01e-4              .01e-5                  78.8
L 1 1    1                    1
                2.4142e7              .01e-4              .01e-5                  78.8
M 1 1    1                    1
                2.4240e7              .01e-4              .01e-5                  78.8
N 1 1    1                    1
                2.4338e7              .01e-4              .01e-5                  78.8
O 1 1    1                    1
                2.4436e7              .01e-4              .01e-5                  78.8
P 1 1    1                    1
                2.4535e7              .01e-4              .01e-5                  78.8
Q 1 1    1                    1
                2.4574e7              .01e-4              .01e-5                  78.8
R 1 1    1                    1
                2.4583e7              .01e-4              .01e-5                  78.8

GENER----1----*----2----*----3----*----4----*----5----*----6----*----7----*----8
F 1 1inj 1                          COM1 1.0000E-06
F 1 1inj 1                          COM3 3.1688E-01
G 1 1inj 1                          COM1 1.0000E-06
G 1 1inj 1                          COM3 1.2675E+00
H 1 1inj 1                          COM1 1.0000E-06
H 1 1inj 1                          COM3 3.1688E+00
I 1 1inj 1                          COM1 1.0000E-06
I 1 1inj 1                          COM3 3.1688E+00
J 1 1inj 1                          COM1 1.0000E-06
J 1 1inj 1                          COM3 3.1688E+00
K 1 1inj 1                          COM1 1.0000E-06
K 1 1inj 1                          COM3 3.1688E+00
L 1 1inj 1                          COM1 1.0000E-06
L 1 1inj 1                          COM3 3.1688E+00
M 1 1inj 1                          COM1 1.0000E-06
M 1 1inj 1                          COM3 3.1688E+00
N 1 1inj 1                          COM1 1.0000E-06
N 1 1inj 1                          COM3 3.1688E+00
O 1 1inj 1                          COM1 1.0000E-06
O 1 1inj 1                          COM3 3.1688E+00
P 1 1inj 1                          COM1 1.0000E-06
P 1 1inj 1                          COM3 3.1688E+00
Q 1 1inj 1                          COM1 1.0000E-06
Q 1 1inj 1                          COM3 1.2675E+00
R 1 1inj 1                          COM1 1.0000E-06
R 1 1inj 1                          COM3 3.1688E-01

TIMES----1----*----2----*----3----*----4----*----5----*----6----*----7----*----8
   51   51
    1.0E-63.1558E+076.3115E+079.4673E+071.2623E+081.5779E+081.8935E+082.2090E+08
2.5246E+082.8402E+083.1558E+083.4713E+083.7869E+084.1025E+084.4181E+084.7336E+08
5.0492E+085.3648E+085.6804E+085.9959E+086.3115E+086.6271E+086.9427E+087.2582E+08
7.5738E+087.8894E+088.2050E+088.5206E+088.8361E+089.1517E+089.4673E+089.7829E+08
1.0098E+091.0414E+091.0730E+091.1045E+091.1361E+091.1676E+091.1992E+091.2307E+09
1.2623E+091.2939E+091.3254E+091.3570E+091.3885E+091.4201E+091.4516E+091.4832E+09
1.5148E+091.5463E+091.5779E+09

ENDCY----1----*----2----*----3----*----4----*----5----*----6----*----7----*----8
```